This manuscript is a non-peer reviewed preprint submitted to EarthArXiv. A copy of this manuscript has been submitted in Earth and Planetary Science Letters (Elsevier). Currently in-revision.

Periodicity in the Deccan volcanism modulated by plume perturbations at the mid-mantle transition zone

Dip Ghosh[1], Joyjeet Sen[2], and Nibir Mandal[3]

Department of Geological Sciences, Jadavpur University, Kolkata 700032, India

Abstract

In peninsular India, the Deccan Traps record massive, continental-scale volcanism in a sequence of magmatic events that mark the mass extinction at the Cretaceous-Paleogene boundary. Although the Deccan volcanism is linked with the Réunion hotspot, the origin of its periodic magmatic pulses is still debated. We develop a numerical model, replicating the geodynamic scenario of the African superplume underneath a moving Indian plate, to explore the mechanism of magmatic pulse generation during the Deccan volcanism. Our model finds a connection between the Réunion hotspot and the African large low shear-wave velocity province (LLSVP) to show pulse generation from a thermochemical plume in the lower mantle. The plume is perturbed at 660 km, and its head eventually detaches from the tail under the influence of Indian plate movement to produce four major pulses (periodicity: $5-8$ Ma), each giving rise to multiple secondary magmatic pulses at a time interval of ~ $0.15-0.4$ Ma.

Keywords: Deccan Traps; Cretaceous-Paleogene extinction; Numerical simulation; African LLSVP; Réunion hotspot; Mid-mantle transition.

For correspondence:

[1]dipghosh14@gmail.com ; [2]senjoyjeet@gmail.com; [3]nibir.mandal@jadavpuruniversity.in

1. Introduction

Deccan Traps (DTs), the most spatially extensive continental flood basalt (CFB) province in peninsular India, witness a remarkable event of volcanism in the Phanerozoic history of the Earth (Chenet et al., 2009), which in recent times has received particular attention in connection with the mass extinction of biological species (Keller et al., 2012; Wilson, 2014). A school of thought relates this sudden biotic crisis to the enormous volume (> 10^6 km^3) of basaltic magma eruptions in the Deccan provinces (Schoene et al., 2015; Wignall, 2001) during late Mesozoic to early Cenozoic (Fig. 1a). This massive volcanism involved degassing on a global scale, resulting in two significant environmental changes: the first being global warming, carbon cycle disruption, and ocean acidification (Self et al., 2014) associated with volatile emissions, with the second a poisoning of the entire ecosystem (Schmidt et al., 2016) associated with SO_2 injection into the upper atmosphere. Another school of thought has proposed a Chicxulub bolide impact theory for the Cretaceous mass extinction (Alvarez et al., 1980; Schulte et al., 2010), but the issue is still debated. The DTs have also stimulated discussions on the long-standing critical question about the origins of large igneous provinces (LIPs) (Campbell and Griffiths, 1990; Dannberg and Sobolev, 2015; Farnetani and Richards, 1994). What is the potential source of enormous magma supply to LIPs, and how are they connected to lower mantle dynamics (Glišović and Forte, 2017; White and McKenzie, 1995)? This Deccan volcanic province is excellent for studying LIPs as it is relatively young and geographically extensive thus, allowing geoscientists to reliably reconstruct the eruption events in space and time.

Based on volcanological and geochemical properties, the Deccan Volcanic Province (DVP) is divided into three principal stratigraphic successions: Kalsubai, Lonavala, and Wai subgroups (Fig. 1b). The volcanic event that defines the Cretaceous-Paleogene boundary (KPB) at 66.043 ± 0.043 Ma (Sprain et al., 2018) occurred $\sim 165 \pm 68$ ka after the emplacement of Kalsubai falls within Khandala, Bushe, or Poladpur Formations (Richards et al., 2015). Using $^{40}K/^{40}Ar$ plagioclase geochronology of erupted basalts and U-Pb geochronology of zircon from intervening ash beds, several workers have constrained the timings of multiple eruptions pulses (Keller et al., 2012; Richards et al., 2015; Schoene et al., 2019, 2015). All these studies agree that the main eruption phases started shortly before the C30n-C29r geomagnetic reversal and ended following the C29r-C29n reversal. Above the KPB, the Wai subgroup consists of geochemically and volcanologically distinct formations, which suggest more voluminous eruptions (Renne et al., 2015; Richards et al., 2015; Sprain et al., 2019).

This study aims to explore the mechanism of unsteady eruption dynamics in the evolution of DVP through multiple pulses, punctuated by quiescent periods. Previous studies based on geochemical data (Chenet et al., 2007) suggested three phases of DT eruptions, with most of the volume, erupted before the KPB, where the second phase is considered responsible for late Cretaceous environmental changes (Chenet et al., 2009; Petersen et al., 2016) (Fig. 1b,c). Alternative views emphasize the Chicxulub impact to propose that the DVP magma eruptions were mostly a post-KPB event (Renne et al., 2015; Richards et al., 2015). More recent investigations from high-precision U-Pb geochronology (Schoene et al., 2019) report three to four discrete pulses during the main eruption event at KPB, each lasting < 100 ka. The first eruption event that formed the lowermost seven formations lasted from ~ 66.3 to 66.15 Ma ago, followed by the second, third, and fourth pulses at ~ 66.1 to 66.0 Ma, ~ 65.9 to 65.8 Ma, and ~ 65.6 to 65.5 Ma to form the Poladpur Formation, the Ambenali Formation, and the uppermost Mahabaleshwar Formation, respectively (Schoene et al., 2019).

A spectrum of geophysical and geochemical studies finds a linkage of the DVP events with the Réunion hotspot (Bredow et al., 2017; Fontaine et al., 2015; Ganerød et al., 2011). Geochemical proxies suggest a link of the source of Deccan basalts to ocean island basalts

(OIB), actively erupting on the island of La Réunion (Peters and Day, 2017). Glisovic et al., 2017 based on their geophysical model, predicted a deep mantle origin of DVPs and proposed a mantle plume hypothesis to show its connection with the Réunion hotspot. Interestingly, the temporal coincidence of the Deccan volcanic events with the plume-induced accelerated motion of the Indian plate further strengthens the mantle-plume hypothesis proposed for the origin of Deccan CFB (Cande and Stegman, 2011; Glišović and Forte, 2017). Moreover, like Iceland and Tristan da Cunha, the Réunion hotspot is thought to have originated from a laterally vast thermochemical pile above the core-mantle boundary (CMB) beneath present-day Africa, referred to as the African large low shear-wave velocity province (LLSVP) (Tsekhmistrenko et al., 2021). This pile might have transported primordial material from CMB to the surface via Réunion and other plumes, as evident from geochemical studies on Sr-Nd-Os systematics (Peters and Day, 2017). Although geophysical and geochemical evidence suggests a connection between the Réunion hotspot and African LLSVP, the mechanism of episodic Deccan volcanism is still unknown.

In this article we examine the thermochemical scenario that favours the Réunion hotspot to operate in pulsating fashion with characteristic periodicity, producing a huge cumulative volume of Deccan basalt at the KPB. We then show how a single major pulse can give rise to a number of secondary pulses of smaller timescales, as reflected from volcanic episodes in the DVP on time scales less than a million years (Ma). Our thermochemical model allows us to constrain a spectrum of the periodicity timescales (a few Ma to less than a Ma), depending on the thermomechanical properties of the source materials. We present a budget for the volume flux from the mantle to the surface.

2. Methods

2.1. Model set-up

The developer version of finite element code ASPECT 2.4.0 (Dannberg and Heister, 2016; Heister et al., 2017) is used to develop our thermochemical model, treating the mantle as a system of stratified fluid layers with their density and viscosity varying as a function of pressure, temperature, composition, and phase transformations. The model domain covers the entire vertical depth (~ 2890 km) of the mantle with a horizontal width of 11560 km, which is discretized into 5.5×5.5 km cells. Since this work primarily aims to study the dynamics and pulsating nature of the plumes, we assume a pre-existing high-density basal layer of a specified thickness of 150 km (Citron et al., 2020) at the CMB given by a single compositional field to represent the pile (Fig. S2). The changes in the composition field are tracked using passive tracers that advect with the global flow. We imposed an initial sinusoidal temperature profile (Citron et al., 2020; Li et al., 2018) in the background mantle to initiate convection and two thermal boundary layers (TBL) using error functions at the top and the bottom of the domain to represent the CMB TBL and the lithosphere, respectively (Fig. S2c). In addition, heat is introduced into the system by internal heating within the pile (Fig. S2b). We considered heating rate up to 20 times that in the background mantle.

To calculate the physical parameters of different model components, we use a *depth-dependent* composite material model built in the ASPECT material library. All material properties are assigned from an incompressible *base model*; this model assumes constant parameter coefficients to represent the ambient mantle values, except for the density and viscosity. We use the depth-dependent material model to describe the different viscosities assigned for the lithosphere and upper and lower mantle. Additionally, we consider the thermal and compositional pre-factors to vary the viscosity as a function of temperature and composition. Density varies mainly due to both thermal expansion and compositional variations in our model. The depth-dependent density function also accounts for phase transitions in the ambient mantle and the basal layer. We varied the excess density of the basal layer (pile) from 150 to 450 kg/m^3 and its viscosity from 0.1 to 100 times that of the ambient mantle (Fig. S2 a-d).

The top and bottom model boundaries are subjected to isothermal conditions with T = 298K and T = 3300K, respectively (Fig. S2c). A uniform velocity condition is imposed at the top boundary of the initial model, keeping all other boundaries under a free-slip condition. We reset the boundary conditions of our model to accommodate the temporal variation of plate velocity, to replicate the plate motion history using the plate motion model from previous studies (Seton et al., 2012). A comprehensive list of the model parameters is provided in Table 1. To determine the physical properties of sequential plume surges, we consider a line segment across the model box length at a depth of 400 km, which lies above the plume-pulses initiation depth. We then find excess or deficit of physical properties from the peak amplitude from the curve with respect to the background value representing the ambient mantle (Fig. S4).

To develop partial melting models, we used a 2D Cartesian box with a vertical depth of 350 km from Earth's surface and a horizontal length of 700 km (Fig. S5a). The dimensions are reduced to achieve a high-resolution analysis of the melting phenomena. Unlike the whole mantle model, here, we consider the compressibility of both the solid and the melt phases within a two-phase model. The top thermal boundary layer represents the thermal structure of the Indian shield during the Late Mesozoic with a LAB depth of ~160 km. A thermal perturbation of 250-500 K is added at the bottom boundary to represent the excess temperature (non-adiabatic temperature) derived by the plume head from the whole mantle model (Fig. S5b ii). The boundary velocity condition is the same as in the previous model, except for the bottom boundary, where mass can flow in and out, thus supplying plume material to generate successive melt pulses. Initially, the system is considered to be free from porosity. We used mesh deformation at the upper boundary to track the surface topography generated in the successive melting events. The details of the model parameters is given in Table 2.

2.2. Problem formulation

Our 2D thermochemical convection simulations are developed in a theoretical framework of Boussinesq approximation, using mass, momentum, and energy conservation equations:

$$\nabla \cdot \mathbf{u} = 0, \tag{1}$$

$$\nabla P - \nabla \cdot [\mu_r \dot{\epsilon}] = \Delta \rho g \mathbf{e_z}, \tag{2}$$

$$\rho_0 C_P \left(\frac{\partial T}{\partial t} + \mathbf{u} \cdot \nabla T \right) - \nabla \cdot K \nabla T = \rho_0 H, \tag{3}$$

where $\mathbf{u}$, P, μ_r, $\dot{\epsilon}$ denote the following physical variables: velocity, dynamic pressure, viscosity, and strain rate, respectively. g is the gravitational acceleration, ρ_0 is the reference density of the ambient mantle, C_P is the specific heat at constant pressure, and T, K, and H are the absolute temperature, thermal conductivity, and the rate of internal heating, respectively.

To replicate Earth-like convective vigor, we choose a set of parameters to appropriately fix the reference Rayleigh number for the mantle:

$$Ra = \frac{\rho_0 g \alpha_0 \Delta T z^3}{\kappa_0 \mu_0}, \tag{4}$$

α_0, κ_0 and μ_0 represent the reference values of the coefficients of thermal expansion, the thermal diffusivity, and the viscosity of the ambient mantle, respectively. The basal layer has a density difference with the ambient mantle, which is introduced in our modelling as Buoyancy number:

$$B = \frac{\Delta \rho}{\rho_0 \alpha_0 \Delta T}, \tag{5}$$

B expresses the intrinsic density anomaly normalized to that caused by thermal expansion.

Discontinuous Galerkin method is used in ASPECT to implement tracking of compositional fields. The advection of composition is given by

$$\frac{\partial \overline{c}}{\partial t} + (\mathbf{u}.\nabla \overline{c}) = 0, \tag{6}$$

where $\overline{c}$ is the compositional vector.

The density and viscosity in the material model vary according to the following equations.

$$\mu_b(p, T, \overline{c}) = \tau(T)\zeta(\overline{c})\mu_0, \tag{7}$$

$$\rho_b(p, T, \overline{c}) = \big(1 - \alpha(T - T_0)\big)\rho_0 + \Delta\rho c_0, \tag{8}$$

where μ_b and ρ_b are the viscosity and density calculated from the base model; μ_0 and ρ_0 denote their corresponding reference values. α is the coefficient of thermal expansion, $\Delta\rho$ is the density difference between the source layer and the ambient mantle, c_0 stands for the first component of the compositional vector $\overline{c}$. The temperature pre-factor in eq. 7 is expressed as

$$\tau(T) = H_T \exp\left(-\frac{A(T - T_0)}{T_0}\right), \tag{9}$$

where A is the thermal viscosity exponent, and

$$H_T = \begin{cases} \tau_{min} & \text{if } \varphi < \tau_{min}, \\ \varphi & \text{if } 10^{-2} < \varphi < 10^{2}, \\ \tau_{max} & \text{if } \varphi > \tau_{max}, \end{cases} \tag{10}$$

$\varphi = \exp(-A(T - T_0)/T_0)$. τ_{min} and τ_{max} represents the minimum and the maximum values of the thermal pre-factors, respectively. The compositional pre-factor in eq 7 is taken in the form:

$$\zeta(\overline{c}) = \xi^{c_0}, \tag{11}$$

ξ is the compositional viscosity pre-factor corresponding to composition c_0. From a depth-dependent model, we find model viscosity:

$$\mu(z, p, T, \overline{c}, \dots) = \frac{\mu(z)\mu_b(p, T, \overline{c}, \dots)}{\mu_0}, \tag{12}$$

where $\mu(z)$ is the depth-dependent viscosity calculated from a depth-dependent model.

Depth dependent phase transition is defined in ASPECT, the expression of which follows,

$$\Gamma = 0.5\left(1 + \tanh\left(\frac{\Delta p}{w}\right)\right), \tag{13}$$

w denotes the phase-transition zone width. Δp is the pressure difference across the width of phase transition zones, given by

$$\Delta p = z - z_{transition} - \gamma(T - T_{transition}), \tag{14}$$

where γ is the Clapeyron slope.

ASPECT calculates the dynamic topography from the stress at the surface in the following way. First, it evaluates the stress component that acts in the direction of gravity at the centres of the cells along the top model surface. The dynamic topography is then calculated using,

$$h_{dt} = \frac{\sigma_{rr}}{(\mathbf{g}.\mathbf{n})\rho}, \tag{15}$$

where h_{dt} is the dynamic topography, σ_{rr} is the stress calculated in the previous step, ρ is the density of the corresponding cell center, and $\mathrm{g}.\mathrm{n}$ is the component of gravity.

The melting model is implemented in ASPECT by separating out the fluid phase from its solid counterpart, which is related by compaction pressure as,

$$p_c = (1 - \phi)(p_s - p_f), \tag{16}$$

where ϕ is porosity, p_s is the solid pressure and p_f is the fluid pressure. After computing the stokes equation, the fluid velocity is calculated from Darcy's equation,

$$u_f = u_s - \frac{K_D}{\phi}\left(\nabla p_f - \rho_f g\right), \tag{17}$$

where u_f is the fluid velocity and u_s is the solid velocity, K_D is the Darcy coefficient, and ρ_f is fluid density. The porosity is advected using the following relation,

$$\frac{\partial \phi}{\partial t} + u_s \cdot \nabla \phi = \frac{\Gamma}{\rho_s} + (1-\phi)\nabla . u_s, \tag{18}$$

Γ is the rate of melting. Permeability is then calculated from

$$k_\phi = k_0 \phi^2 (1-\phi)^3, \tag{19}$$

k_0 is the reference permeability.

3. Results

3.1. Pulsating rise of thermochemical plumes

We consider pile density, viscosity, concentration of heat-producing elements (HPE), and major phase transitions in the mantle to obtain a reasonable plume model for the Deccan LIP evolution in the geodynamic framework of the Réunion hotspot. In this modelling, the buoyancy number (B), which measures density contrast of the pile with the ambient lower mantle, accounts for varying relative proportions of eclogite and peridotite within the basal layer. As the viscosity and heat-producing element concentration of the pile are not well constrained, we varied them within a plausible range of their values found in the literature (Citron et al., 2020; Dannberg and Sobolev, 2015; Heyn et al., 2020; Li et al., 2018). A velocity boundary condition is imposed at the upper model boundary to replicate the lithospheric plate kinematics that prevailed during Réunion hotspot activities. The details of the model domain and parameters used for the simulations along with the initial model boundary conditions are provided in the Methods section and Supplementary Figs. S1, S2.

The plate velocity induces downwelling flow in the mantle, which forces the thermal boundary layer (TBL) at the CMB to pile up laterally and increase its thickness (h_{TBL}~300 km) (Fig. S3a). The TBL is pushed towards the pile to increase h_{TBL} further (Fig. S3b), amplifying the Rayleigh number (Ra) in the TBL to locally exceed the critical Ra. Under this threshold condition, the buoyancy head becomes high enough to force the material to flow vertically against gravity, forming a thermochemical plume (Figs. S3c, d). Due to its strong buoyancy flux, the plume grows mainly in the vertical direction within the lower mantle. However, on encounter with the upper mantle, it faces two processes that significantly hinder its continuous growth: 1) influence of the plate velocity and 2) phase transition between 300 and 400 km (Dannberg and Sobolev, 2015). At this stage, the plate-driven flow extends to a depth of 660 km and exert drags to the plume head (Fig. S3e), detaching it from the tail counterpart. The buoyancy ultimately takes over the drag, allowing the head to move vertically upward in the form of a solitary pulse (Figs. 2a i-iv). The ascending head undergoes phase transformations: coesite to stishovite and pyroxene to garnet, increasing the plume density. Ultimately, inherent high excess temperatures enable plumes to overcome this density-enhancing barrier to reach the lithosphere-asthenosphere boundary (LAB), where they spread laterally in the horizontal direction. This stagnation process facilitates thermal mixing and mechanical entrainment within the mantle.

The model run shows that the plume upwells in a pulsating fashion to produce multiple heads in the course of the ascent event (Figs. 2a i-iv). The primary head gives rise to the first pulse following its detachment from the main body after crossing the 660 km boundary (Fig. 2a i). The initiation of the plume destabilizes the pile margin (Figs. 2a i, ii), as indicated by reducing pile volumes and high rates of its lateral migration (~ 10 km/Ma) (Figs. 2b ii, iii), that produces relatively high eclogite proportions (~ 10%) and heat-producing element concentration in the plume (Fig. S4a). A large buoyancy head due to the high excess temperature (> 500 K) and density contrast (> -50 kg/m^3) (Figs. S4b, c) facilitates the surface to attain high dynamic topography with an elevation of ~1600 m (Fig. 2a i inset) and inflates the pulse volume ($\sim 1.5 \times 10^7$ km^3) (Fig. 2b i). The pile margin remains unstable (Fig. 2a ii), forcing a large volume of material to upwell through the plume tail and produce a second pulse (Fig. 2b ii) as time elapses after the first pulse allowing new materials to accumulate in a threshold volume at 660 km. Unlike the first pulse, the second pulse evolves with a moderate amount of eclogite and heat-producing elements (HPE) to form significantly lower pulse volume (0.9×10^7 km^3) and dynamic topography (~800 m) (Fig. 2a ii inset) owing to its lower excess temperature (~400 K) and density contrast (> -40 kg/m^3) (Figs. S4b, c). With time the pile moves further away from the plume axis but the rate of the movement reduces to ~5-6 km/Ma. It sustains the periodic material supply to the 660 km boundary to produce tertiary pulses (Figs. 2a iii, iv; 2b iii). The pile eventually attains a stable state, and unstable to stable transition results in a drastic reduction in material volume supply to the plume (Fig. 2b ii), marked by much lower pulse volume ($\sim 0.5 \times 10^7$ km^3) and a low positive dynamic topography (~100-200 m) (Figs. 2a iii, iv insets) with low excess temperature (~ 250 K) and density contrast (~-20 kg/m^3).

Although all the sequential pulses ultimately reach the LAB and take part in melting and subsequent volcanism, the primary (first) pulse, owing to its sufficient excess temperature (> 500 K), and volume ($\sim 1.5 \times 10^7$ km^3) takes the lead role in forming LIPs. The thermochemical pile, which is the primary material feeder for the pulses, stratifies a specific set of physio-chemical parameters to generate a reasonable melt volume and dynamic topography required for the formation of Deccan LIP.

3.2. Buoyancy effects on plume rise dynamics

We performed a series of simulations to investigate how the buoyancy number (B) of the pile influenced the process of pulse generation at the mid-mantle transition zone for a given viscosity ratio (μ ~1) and HPE concentration. For low B values ($<$ 1), the mantle flow efficiently drags the pile horizontally to widen the exposed CMB fraction, causing both h_{TBL} and pile height (h_{pile}) to increase at high rates (Figs. 3a, c; 4a). Consequently, the pile becomes unstable (Fig. 3a) to accelerate material flux into the plume and gives rise to initial pulses with large volumes ($> 1.5 \times 10^7$ km^3) and dynamic topography (> 1500 m) (Figs. 3a, c inset; Fig. 4b). Increasing B weakens the interaction of mantle flow with the pile due to a high intrinsic density of the basal layer, leading to TBL thickening at slow rates. (Figs. 3b, d; Fig. 4a). As a result, the plume having the same initial excess temperature produces pulses of much smaller volumes ($< 1.1 \times 10^7$ km^3) (Fig. 4b) and dynamic topography (<1100 m) (Figs. 3b, d insets). Moreover, the volume difference in primary, secondary, and tertiary pulses are much more pronounced at a lower B value (Fig. 4a).

3.3. Viscosity effects on pulse-driven processes

Geophysical studies suggest that the viscosity of thermochemical piles can be up to 1000 times higher than the ambient mantle (Heyn et al., 2020). We find that an increase in the viscosity ratio (μ) from 1 to 100 considerably dampens the vertical growth of piles, allowing them to remain stable for given values of B and HPE concentration (Fig. 3e-h), as reflected from the lower rates of pile volume changes (Fig. 4c). This increase in μ, on the other hand, strengthens the interaction of mantle flow with the pile, as evidenced from large exposed CMB areas (Fig. 4a). Such a strong interaction increases the horizontal shortening of the pile at the cost of vertical growth, eventually reducing pulse volumes by up to 12 % (Fig. 4b) and widening the time periodicity of pulse generation. μ also significantly influences the dynamic topography. The model estimates for $\mu = 1$ yield a large dynamic topography (> 3000 m) when B is low (< 0.8), which is considered unrealistic for thermochemical plumes. Increasing μ to 100 depresses the topography to < 2000 m for lower values of B which can be correlated with Deccan volcanic events.

3.4. Effect of internal heat production on plume dynamics

Geochemical observations on OIBs support the presence of enriched mantle reservoirs as mantle heterogeneity and/or variable mantle reservoirs (Peters and Day, 2017). Some of these sources are less degassed and hence, are more enriched in HPEs. One possibility is that such reservoirs could be present within LLSVPs since they are primarily composed of primordial material, subducted Hadean crust, or recycled oceanic crust remnants from a decomposed subducted plate (Deschamps et al., 2011). Previous estimates, based on heat budget calculations, show that the heat-producing element concentrations (c_{HPE}) can be as high as 20 to 25 times that of the background mantle (Citron et al., 2020). To study the role of this factor on the pile dynamics, we increased c_{HPE} of the pile by up to 20 times that of the ambient lower mantle. Such enrichment augments the pile buoyancy with time to set a gravitationally unstable state of the pile even under a high B condition. Plumes that originate from pile edges in our models entrain HPE-enriched pile materials to increase its excess temperature. However, c_{HPE} has relatively weak effects, as compared to other parameters, such as viscosity ratio (μ) (Figs. 3 c-d, g-h). c_{HPE} primarily affects the dynamic topography and, more importantly, the material supply to thermochemical plumes (Figs. 4b, c). Increase in c_{HPE} amplifies the dynamic topography and also enhances material supply to the plume, especially at a lower value of the buoyancy number (B). The other remarkable effect of c_{HPE} on plume geometry is that the plume develops a thick tail, which facilitates pile material transport to the mid-mantle region in larger volumes (Fig. 3g), compared to that produced in a lower c_{HPE} condition. This is also reflected in higher rate of reduction in pile volumes with time (Fig. 4c), which implies a more effective pile material entrainment into the plume tail. In addition, high c_{HPE} causes the plume to gain a higher excess temperature that results in dynamic topography with a realistic elevation of ~1600 m for the primary pulse for μ = 100 (Fig. 3g inset).

3.5. Melt transport from a thermochemical plume

When the plume head approaches the LAB, the temperature inside the plume exceeds the local solidus to initiate the melting process in the plume materials. This phenomenon inevitably increases the porosity of the system, which thereby enhances permeability in the top region of the plume head (Fig. S6). The Indian shield (a stable craton) had a thickness of 150-200 km before it started to interact with the plume (Naganjaneyulu and Santosh, 2012), implying a deep upper thermal boundary layer. Depending upon the initial temperature, composition, and volume of the plume head, the melting process is onset at a depth varying from ~ 150 to 250 km. During the initial phase of ascent, the magnitudes of melt and plume velocities lie compatibly in a range of $0.4 - 0.6\ \mathrm{m/year}$ (Fig. S5b i), but as the plume ascends to a shallower depth, the melts owing to their lower density (2700 kg/m^3), gain a much higher velocity (> 1.2 m/year) to segregate from the plume materials at the LAB (Fig. S5b v). Our model results suggest that the melt-ascent velocity is directly proportional to the porosity in the system, which increases steadily with the plume evolution. Unlike the plume head, the segregated melts always ascend nearly in a vertical direction, implying that the plate velocity hardly affects the upward melt flow dynamics. At a depth of ~60-80 km, the segregated melts start to spread laterally, forming a melt pool below the lithosphere (a permeability barrier) (Fig. 5a). The melt front interacts with the lithosphere to produce horizontal shear that sets in small-scale downwelling and causes thinning of the TBL. Upwelling of the melt front within the lithosphere ultimately gives rise to volcanism. We evaluated the melt volume, velocity, time scale of the melt rise, and dynamic topography as a function of the initial plume volume, temperature, and density, which are presented in Fig. 5 and Fig. S5b.

Since the primary plume pulse has the highest volume (~1.5×10^7 km^3), it contains a high concentration of HPEs. This condition, aided with a high excess temperature (~500 K) (Fig. S5), enables the pulse to overcome the upper-mantle buoyancy barriers. Model results show that the higher excess temperatures and HPE concentrations result in a greater melting depth (~250 km) of the initial melt pulse (Fig. 5a i), and also enhance the excess buoyancy, that accelerates the upward flow of melts to reach a depth of 50 km within 150-180 kyr (Fig. 5b). The porosity evolution, coupled with a high excess temperature, facilitates melt generation during the plume ascent to produce an enormous volume ($\sim 0.28 \times 10^6$km^3) of melts at the LAB (Fig. 5b). This melt pool then efficiently incorporates lithospheric materials by thermal erosion to increase the melt volume further ($\sim 0.35 \times 10^6$km^3), ultimately giving rise to massive volcanism. Following this melt pulse generation, the plume head is then significantly depleted in HPE concentration. Secondly, the heat dissipation to the ambient mantle lowers the excess temperature (~300 K) in the plume. The thermal change by these mechanisms relocates the melting depth at a shallower level (150 to 180 km) during the subsequent pulses, where a moderate excess temperature, a relatively low HPE concentration, and smaller plume volume set the upward melt flows at slow rates ($\sim$ 0.5 m/year), taking up to 300 kyr to reach the LAB. These second-generation pulses reduce their melt volumes to $< 0.2 \times 10^6$ km^3. In addition, the thermal erosion of the lithosphere at the LAB by the melt pools becomes less effective and fails to substantially increase the melt volumes (Fig. 5a ii). Thus, they produced erupted volumes significantly lower than those produced in the first pulse. The smaller pulses are manifested in relatively low topographic elevations (Figs. 5b, c). The tertiary melt pulses further reduce their volumes and their excess temperatures (~ 250 K) and lose their capacity for large-scale thermal erosion of the lithosphere and attaining a stagnation state at a depth of ~50 km (Fig. 5a iii).

4. Discussion

4.1. Deccan volcanism - African superplume connection

It is now a well-accepted hypothesis that the existence of African LLSVP dates back to at least the Pangea event (Zhang et al., 2010). During the Gondwana-proto-Laurussia convergence, several cold subducting slabs assembled in the lower mantle beneath the African continental lithosphere to form this distinct layer above the CMB, whose current location and shape have been framed in the post-Pangea subduction history. Recent mantle convection models coupled to continuously evolving plate boundaries (Hassan et al., 2016; Müller et al., 2016) track the African LLSVP positions through time, considering the subduction driven mantle flow due to Neo-Tethys Ocean closure, as illustrated in Fig. 6a, b. The model results suggest that the western margin of African LLSVP remained almost stable during the entire Cretaceous period, but the eastern flank has continuously relocated its position. The time-dependent effect of subduction on the north (closure of Tethys) produced a strong southward lower-mantle poloidal flow (Fig. 6a), leading to mantle upwelling in the south. The upwelling dynamics, in turn, induced a convective mantle "roll" that forced the eastern flank of the African LLSVP boundary to migrate southward and the Indian plate to move northward at a higher velocity (Glišović and Forte, 2017). These interpretations are further validated by geophysical observations that predict deformation and southward movement of the African LLSVP under east Africa (Ford and Long, 2015).

Our modelling domain considers a north-south cross-section of the mantle to replicate the Indian plate movement in late Mesozoic and Cenozoic (past 130 Ma) and reconstruct the eastern flank position of the African LLSVP relative to the Indian subcontinent (Fig. S1). The model simulations suggest that a large mantle roll, formed as a consequence of the subduction in the north (*cf.* Glisovic et al., 2017), forced the pile to move in the southward direction at a rate of 17-19 km/Ma at the beginning of the Late Cretaceous (Fig. 6c ii). This postulate is consistent with the inferences from other studies that claimed the southward movement of African LLSVP due to the presence of deep-mantle southward poloidal flow as a consequence of the Tethyan subduction over the past 130 Ma (Hassan et al., 2020). The poloidal flow resulted in a thermal instability within the exposed CMB on the north of the LLSVP, which subsequently migrated towards the African LLSVP and amplified the pile at its eastern flank to attain a thickness of ~800-1000 km (Fig. S3). The laterally migrating TBL instabilities climbed up the pile edge to reach the crest and finally formed a mature plume. The positional reconstruction of the African LLSVP and the Indian plate for this time period allows us to conclude that the eastern flank of African LLSVP coincided with the Indian plate location in a time frame of 70-65 Ma (Fig. 6b). This plume then generated successive pulses upon reaching the mid-mantle transition zone through the late Mesozoic and Cenozoic, where the first pulse corresponds to the Deccan events at 66 Ma. The plume initiation decelerated the southward pile migration to ~ 6-7 km/Ma (Fig. 6c ii) because the plume forced pile materials to effectively upwell in the vertical direction. Subsequently, the pile migrated further south-westward, whereas the Indian plate had north-eastward movement.

The plume continued to form periodically the secondary and tertiary pulses at mid-mantle depth at an interval of 5-8 Ma, giving rise to successive eruptions from the Réunion hotspot. The plume process eventually reduced pulse volumes and involved a sharp change in the chemical characteristics of the Réunion lava flows during the post-Deccan volcanism period (Peters and Day, 2017). With time, the eastern margin of the pile shifted its position further southwest to reach its current location (Fig. 6b). The present model suggests that the process of sequential plume-head detachment at the mid-mantle transition zone modulated the periodic pulse generation and determine the time scale, volume, and topography associated with each of these pulses. Considering a CMB temperature of 3300 K and an initial pile thickness of 150 km, the model results for B in a range $0.8 - 1.2$ yield a periodicity of 5-8 Ma, similar to that of Réunion activity throughout the Cenozoic. To tally the dynamic topography, the pile also needs to be ~ 100 times viscous ($\mu \sim 100$) and ~ 20 times HPE enriched than the ambient lower mantle. This condition produces a primary pulse volume of $14 - 15.5 \times 10^6$ km^3 and dynamic topography of ~ 2000 m related to the Deccan event, followed by the next generation of pluses with volumes of $\sim 12 \times 10^6$ km^3, $\sim 7 \times 10^6$ km^3, $\sim 3.5 \times 10^6$ km^3 (Fig. 4a) and topography of ~ 1400 m, ~ 700 m, and ~ 200 m.

4.2. The Deccan volcanic periodicity

To study the time periodicity of Deccan volcanism, we focus on the melting process in the primary plume head obtained from our thermochemical model (Fig. 5; Fig. S5). The model results suggest that the plume head locally underwent melting within the asthenosphere to create three eruptive events within a time scale of 1 Ma, where the first event occurred within 0.15 Ma from the plume head stagnation with a cumulative volume of 0.32×10^6 km^3 (Fig. 5b), correlated with the lowermost seven formations produced during the period ~ 66.5-66.3 Ma. The second event took place after a quiescent period of ~ 0.3 Ma with a volume of 0.18×10^6 km^3, which corresponds to the ~ 66.0 Ma Poladpur Formation. Finally, the third pulse that initiated after 0.4 Ma produced a volume of 0.15×10^6 km^3, which can be equated with the Ambanali and later formations deposited during ~ 65.6-65.3 Ma. Based on these model calculations, we estimate a volume flux of ~8-9 km^3/year for the first event, subsequently reduced to $\sim 5 - 5.5$ km^3/year and $\sim 4 - 4.5$ km^3/year, respectively, for the second and third events. This estimate implies that the rate of Deccan volcanic eruption in a pulse (time scale $\leq$ 100 Ka) exceeded the global value (3 to 4 km^3/year) by a factor of 1.5 to 3. Moreover, there must be hiatuses in the order of tens of thousands of kiloyears within the pulses to balance the total volume estimates. Geochemical proxies also suggest a sharp increase of mantle contributions to later volcanic formations, such as Poladpur and Ambenali, indicating a reduction of magma-crust interface area (Renne et al., 2015). The higher rates of thermal erosion at the LAB during the first two events effectively thinned the lithosphere and weakened the vigorousity crust-mantle interaction during the subsequent melt pulse events, as revealed from our models (Fig. 5a).

Although our model estimates broadly agree with the time gaps between different episodes of the Deccan volcanism, they somewhat underestimate the erupted volumes predicted from petrological and geochemical studies (Schoene et al., 2019). Groups of flows within the Poladpur and Mahabaleshwar Formations, each potentially comprising > 50,000 km^3, lack any secular variation of paleomagnetic poles, suggesting the eruption at high rates, $\sim 1000\ \mathrm{km}^3/\mathrm{year}$ on decadal to centuries scales. Our volume and flux estimates for eruptions prior to the KPB tally well with the available data; however, they do not account for either the high melt volumes or the rate of eruption for the post-KPB eruptions. We thus hypothesize that there was a transition in the nature of volcanism across the KPB, the explanation of which demands the possible effects of other internal or external factors. One possible explanation could be that the Chicxulub bolide impact accelerated the eruption rates, as suggested by the previous workers (Renne et al., 2015).

4.3. Comparison with major global LIP events

We will now discuss the Deccan volcanism that occurred sequentially in three major pulses in the context of similar episodic volcanic events from other LIPs and hotspots, such as Hawaii, Réunion, Yellowstone, and others (Morrow and Mittelstaedt, 2021). They show the periodicity of the volcanic events on varied timescales (Fig. 7). For example, the Hawaii-Emperor hotspot track records a sequence of magmatic pulses at around 64 Ma, 50 Ma, 42 Ma, and 28 Ma, implying a pulsating time scale of about 10 Ma (Van Ark and Lin, 2004). On the other hand, from bathymetry analysis Wessel (2016) has established a much shorter pulsating time scale (< 2 Ma) for the post-22 Ma volcanism, as observed in the Deccan volcanism. The Yellowstone LIP started its volcanism at around 18 Ma (Schutt et al., 2008), followed by two distinct magmatic peak events at around 11 Ma and 5 Ma (Stachnik et al., 2008; Waite et al., 2006). In a recent study of the Yellowstone super-volcano, the tomographic P-wave model has detected hot pulses in the upper mantle (Huang et al., 2015). These discrete bodies, most probably pockets of partial melts, represent episodic pulses produced by a large plume source in the mantle, as predicted from our numerical model simulations. The Réunion hotspot displays a major emplacement in Deccan traps at 66-68 Ma, with later magmatic peaks at 57 Ma, 48 Ma, 35 Ma, 8 Ma, and 2 Ma (Mjelde et al., 2010).

4.4. Model limitations

The model presented here treats the lithosphere as an upper thermal boundary layer, which does not account for visco-plastic rheology with a failure criterion, which is a limitation. in our simulations. Secondly, the creep processes that are often activated in the upper mantle could influence the shape and the ascent rate of the plume head, which are not explored in this study. In addition, our primary model excludes any compressibility effect of the solid phases. The plume melting models consider a reaction time scale of 10^3 years due to computational constraints. This might overshoot the overall timescale of melting and melt migration.

5. Summary and Conclusions

The 2D thermochemical simulations demonstrate that the following parameters: pile-ambient mantle viscosity ratio (μ), buoyancy number (B), and heat-producing element concentration (c_{HPE}) have controlled the Réunion hotspot dynamics and its connection to the seismically observed African LLSVP. The position of India is found to match with the African LLSVP location at the end of the Cretaceous Period, where the LLSVP acted as the source of the Réunion hotspot materials to produce the Deccan LIP and subsequent eruption events.

We show that an instability in the TBL above the CMB played a critical role in the Reunion hotspot formation. The instability initiated on the eastern flank of the African LLSVP during the Neo-Tethys subduction (130-150 Ma) but migrated to the pile crest to form a plume. The plume ascent was perturbed at the mid-mantle transition zone to produce four major pulses on a time interval of 5-8 Ma. The model calculations suggest that, at the onset time (Late Cretaceous) of Réunion Hotspot volcanism, the African LLSVP had a Buoyancy number (B) in the range of $0.8 - 1.0$, pile-ambient mantle viscosity ratio (μ) in the order of 100 and heat-producing element concentration (c_{HPE}) 20 times that of the ambient lower mantle. The primary pulse of the Réunion plume had thereby sufficient volumes ($> 1.5 \times 10^7$ km^3) and excess temperature (> 500 K) to produce the Deccan LIPs. The partial-melting model envisages that the primary pulse subsequently gave rise to 3 melt pulses with volumes in the order of ~ $0.15 - 0.35 \times 10^6$ km^3 at a time interval of $0.15 - 0.4$ Ma, as recorded in the Deccan traps.

Finally, we conclude that most of the LIPs evolve in pulses on characteristic time scales, under the influence of combined action of the pile processes operating at the CMB and the feeding mechanism into the plume stem, modulated by a mid-mantle perturbation. The entire sequence of pulses is divided into two categories: major pulses with a periodicity of 5-8 Ma, determined by the plume-head detachment at the mid-mantle transition zone, and minor melt pulses with a 0.15-0.4 Ma time periodicity, determined by the melting phenomenon within each major pulse. The temporal variations in magma eruption characteristics are consistent with depth-dependent compositional heterogeneity of the plume source.

Acknowledgments

This work has been supported by the DST-SERB through the J. C. Bose fellowship (SR/S2/JCB-36/2012) to NM. We thank the Computational Infrastructure for Geodynamics (geodynamics.org) which is funded by the National Science Foundation under awards EAR-0949446 and EAR-1550901 for supporting the development of ASPECT. D.G. and J.S. are thankful to Juliane Dannberg for helpful discussions. We especially thank Dr. Simon Gatehouse, BHP who critically read an earlier version of this manuscript and provided many constructive suggestions.

Data availability

The model parameters required to produce the results are given in the tables and the supplementary information. The simulation code is freely available online under the terms of the GNU General Public License at https://github.com/geodynamics/aspect. Parameter files that reproduce the findings of this study are available from the corresponding author upon reasonable request.

References

Alvarez, L., Alvarez, W., Asaro, F., Michel, H. V., 1980. Extraterrestrial Cause for the Cretaceous-Tertiary Extinction. Science (80-.). 208, 1095–1108.

Bredow, E., Steinberger, B., Gassmöller, R., Dannberg, J., 2017. How plume-ridge interaction shapes the crustal thickness pattern of the Réunion hotspot track. Geochemistry, Geophys. Geosystems 18, 2930–2948. https://doi.org/10.1002/2017GC006875

Campbell, I.H., Griffiths, R.W., 1990. Implications of mantle plume structure for the evolution of flood basalts. Earth Planet. Sci. Lett. 99, 79–93. https://doi.org/10.1016/0012-821X(90)90072-6

Cande, S.C., Stegman, D.R., 2011. Indian and African plate motions driven by the push force of the Réunion plume head. Nature 475, 47–52. https://doi.org/10.1038/nature10174

Chenet, A.L., Courtillot, V., Fluteau, F., Gérard, M., Quidelleur, X., Khadri, S.F.R., Subbarao, K. V., Thordarson, T., 2009. Determination of rapid Deccan eruptions across the Cretaceous-Tertiary boundary using paleomagnetic secular variation: 2. Constraints from analysis of eight new sections and synthesis for a 3500-m-thick composite section. J. Geophys. Res. Solid Earth 114. https://doi.org/10.1029/2008JB005644

Chenet, A.L., Quidelleur, X., Fluteau, F., Courtillot, V., Bajpai, S., 2007. 40K-40Ar dating of the Main Deccan large igneous province: Further evidence of KTB age and short duration. Earth Planet. Sci. Lett. 263, 1–15. https://doi.org/10.1016/j.epsl.2007.07.011

Citron, R.I., Lourenço, D.L., Wilson, A.J., Grima, A.G., Wipperfurth, S.A., Rudolph, M.L., Cottaar, S., Montési, L.G.J., 2020. Effects of Heat-Producing Elements on the Stability of Deep Mantle Thermochemical Piles. Geochemistry, Geophys. Geosystems 21, 1–17. https://doi.org/10.1029/2019GC008895

Crameri, F., Shephard, G.E., Heron, P.J., 2020. The misuse of colour in science communication. Nat. Commun. 11, 1–10. https://doi.org/10.1038/s41467-020-19160-7

Dannberg, J., Heister, T., 2016. Compressible magma/mantle dynamics: 3-D, adaptive simulations in ASPECT. Geophys. J. Int. 207, 1343–1366. https://doi.org/10.1093/gji/ggw329

Dannberg, J., Sobolev, S. V., 2015. Low-buoyancy thermochemical plumes resolve controversy of classical mantle plume concept. Nat. Commun. 6, 1–9. https://doi.org/10.1038/ncomms7960

Deschamps, F., Kaminski, E., Tackley, P.J., 2011. A deep mantle origin for the primitive signature of ocean island basalt. Nat. Geosci. 4, 879–882. https://doi.org/10.1038/ngeo1295

Farnetani, C.G., Richards, M.A., 1994. Numerical investigations of the mantle plume initiation model for flood basalt events. J. Geophys. Res. 99. https://doi.org/10.1029/94jb00649

Fontaine, F.R., Barruol, G., Tkalčić, H., Wölbern, I., Rümpker, G., Bodin, T., Haugmard, M., 2015. Crustal and uppermost mantle structure variation beneath La Réunion hotspot track. Geophys. J. Int. 203, 107–126. https://doi.org/10.1093/gji/ggv279

Ford, H.A., Long, M.D., 2015. A regional test of global models for flow, rheology, and seismic anisotropy at the base of the mantle. Phys. Earth Planet. Inter. 245, 71–75. https://doi.org/10.1016/j.pepi.2015.05.004

Ganerød, M., Torsvik, T.H., van Hinsbergen, D.J.J., Gaina, C., Corfu, F., Werner, S., Owen-Smith, T.M., Ashwal, L.D., Webb, S.J., Hendriks, B.W.H., 2011. Palaeoposition of the seychelles microcontinent in relation to the deccan traps and the plume generation zone in late cretaceous-early palaeogene time. Geol. Soc. Spec. Publ. 357, 229–252. https://doi.org/10.1144/SP357.12

Glišović, P., Forte, A.M., 2017. On the deep-mantle origin of the Deccan Traps. Science (80-.). 355, 613–616. https://doi.org/10.1126/science.aah4390

Hassan, R., Müller, R.D., Gurnis, M., Williams, S.E., Flament, N., 2016. A rapid burst in hotspot motion through the interaction of tectonics and deep mantle flow. Nature 533, 239–242. https://doi.org/10.1038/nature17422

Hassan, R., Williams, S.E., Gurnis, M., Müller, D., 2020. East African topography and volcanism explained by a single, migrating plume. Geosci. Front. 11, 1669–1680. https://doi.org/10.1016/j.gsf.2020.01.003

Heister, T., Dannberg, J., Gassmöller, R., Bangerth, W., 2017. High accuracy mantle convection simulation through modern numerical methods - II: Realistic models and problems. Geophys. J. Int. 210, 833–851. https://doi.org/10.1093/gji/ggx195

Heyn, B.H., Conrad, C.P., Trønnes, R.G., 2020. How Thermochemical Piles Can (Periodically) Generate Plumes at Their Edges. J. Geophys. Res. Solid Earth 125. https://doi.org/10.1029/2019JB018726

Huang, H., Lin, F., Schmandt, B., Farrell, J., Smith, R.B., Tsai, V.C., 2015. The Yellowstone magmatic system from the mantle plume to the upper crust. Science (80-.). 348, 773–776.

Kale, V.S., Bodas, M., Chatterjee, P., Pande, K., 2020. Emplacement history and evolution of the Deccan Volcanic Province, India. Episodes 43, 278–299. https://doi.org/10.18814/EPIIUGS/2020/020016

Keller, G., Adatte, T., Bhowmick, P.K., Upadhyay, H., Dave, A., Reddy, A.N., Jaiprakash, B.C., 2012. Nature and timing of extinctions in Cretaceous-Tertiary planktic foraminifera preserved in Deccan intertrappean sediments of the Krishna-Godavari Basin, India. Earth Planet. Sci. Lett. 341–344, 211–221. https://doi.org/10.1016/j.epsl.2012.06.021

Li, M., Zhong, S., Olson, P., 2018. Linking lowermost mantle structure, core-mantle boundary heat flux and mantle plume formation. Phys. Earth Planet. Inter. 277, 10–29. https://doi.org/10.1016/j.pepi.2018.01.010

Mjelde, R., Wessel, P., Müller, R.D., 2010. Global pulsations of intraplate magmatism through the Cenozoic. Lithosphere 2, 361–376. https://doi.org/10.1130/L107.1

Morrow, T.A., Mittelstaedt, E.L., 2021. Quantifying Periodic Variations in Hotspot Melt Production. J. Geophys. Res. Solid Earth 126. https://doi.org/10.1029/2021JB021726

Müller, R.D., Seton, M., Zahirovic, S., Williams, S.E., Matthews, K.J., Wright, N.M., Shephard, G.E., Maloney, K.T., Barnett-Moore, N., Hosseinpour, M., Bower, D.J., Cannon, J., 2016. Ocean Basin Evolution and Global-Scale Plate Reorganization Events since Pangea Breakup. Annu. Rev. Earth Planet. Sci. 44, 107–138. https://doi.org/10.1146/annurev-earth-060115-012211

Naganjaneyulu, K., Santosh, M., 2012. The nature and thickness of lithosphere beneath the Archean Dharwar Craton, southern India: A magnetotelluric model. J. Asian Earth Sci. 49, 349–361. https://doi.org/10.1016/j.jseaes.2011.07.002

Peters, B.J., Day, J.M.D., 2017. A geochemical link between plume head and tail volcanism. Geochemical Perspect. Lett. 5, 29–34. https://doi.org/10.7185/geochemlet.1742

Petersen, S. V., Dutton, A., Lohmann, K.C., 2016. End-Cretaceous extinction in Antarctica linked to both Deccan volcanism and meteorite impact via climate change. Nat. Commun. 7, 1–9. https://doi.org/10.1038/ncomms12079

Renne, P.R., Sprain, C.J., Richards, M.A., Self, S., Vanderkluysen, L., Pande, K., 2015. State shift in Deccan volcanism at the Cretaceous-Paleogene boundary, possibly induced by impact. Science (80-.). 350, 76–78.

Richards, M.A., Alvarez, W., Self, S., Karlstrom, L., Renne, P.R., Manga, M., Sprain, C.J., Smit, J., Vanderkluysen, L., Gibson, S.A., 2015. Triggering of the largest Deccan eruptions by the Chicxulub impact. Bull. Geol. Soc. Am. 127, 1507–1520. https://doi.org/10.1130/B31167.1

Ritsema, J., Deuss, A., Van Heijst, H.J., Woodhouse, J.H., 2011. S40RTS: A degree-40 shear-velocity model for the mantle from new Rayleigh wave dispersion, teleseismic traveltime and normal-mode splitting function measurements. Geophys. J. Int. 184, 1223–1236. https://doi.org/10.1111/j.1365-246X.2010.04884.x

Schmidt, A., Skeffington, R.A., Thordarson, T., Self, S., Forster, P.M., Rap, A., Ridgwell, A., Fowler, D., Wilson, M., Mann, G.W., Wignall, P.B., Carslaw, K.S., 2016. Selective environmental stress from sulphur emitted by continental flood basalt eruptions. Nat. Geosci. 9, 77–82. https://doi.org/10.1038/ngeo2588

Schoene, B., Eddy, M.P., Samperton, K.M., Keller, C.B., Keller, G., Adatte, T., Khadri, S.F.R., 2019. U-Pb constraints on pulsed eruption of the Deccan Traps across the end-Cretaceous mass extinction. Science (80-.). 363, 862–866. https://doi.org/10.1126/science.aau2422

Schoene, B., Samperton, K.M., Eddy, M.P., Keller, G., Adatte, T., Bowring, S.A., Khadri, S.F.R., Gertsch, B., 2015. U-Pb geochronology of the Deccan Traps and relation to the end-Cretaceous mass extinction. Science (80-.). 347, 182–184. https://doi.org/10.1126/science.aaa0118

Schulte, P., Alegret, L., Arenillas, I., Arz, J.A., Barton, P.J., Bown, P.R., Bralower, T.J., Christeson, G.L., Claeys, P., Cockell, C.S., Collins, G.S., Deutsch, A., Goldin, T.J., Goto, K., Grajales-Nishimura, J.M., Grieve, R.A.F., Gulick, S.P.S., Johnson, K.R., Kiessling, W., Koeberl, C., Kring, D.A., MacLeod, K.G., Matsui, T., Melosh, J., Montanari, A., Morgan, J. V., Neal, C.R., Nichols, D.J., Norris, R.D., Pierazzo, E., Ravizza, G., Rebolledo-Vieyra, M., Reimold, W.U., Robin, E., Salge, T., Speijer, R.P., Sweet, A.R., Urrutia-Fucugauchi, J., Vajda, V., Whalen, M.T., Willumsen, P.S., 2010. The chicxulub asteroid impact and mass extinction at the cretaceous-paleogene boundary. Science (80-.). 327, 1214–1218. https://doi.org/10.1126/science.1177265

Schutt, D.L., Dueker, K., Yuan, H., 2008. Crust and upper mantle velocity structure of the Yellowstone hot spot and surroundings. J. Geophys. Res. Solid Earth 113, 1–14. https://doi.org/10.1029/2007JB005109

Self, S., Schmidt, A., Mather, T.A., 2014. Emplacement characteristics, time scales, and volcanic gas release rates of continental flood basalt eruptions on Earth. Spec. Pap. Geol. Soc. Am. 505, 319–337. https://doi.org/10.1130/2014.2505(16)

Seton, M., Müller, R.D., Zahirovic, S., Gaina, C., Torsvik, T., Shephard, G., Talsma, A., Gurnis, M., Turner, M., Maus, S., Chandler, M., 2012. Global continental and ocean basin reconstructions since 200Ma. Earth-Science Rev. 113, 212–270. https://doi.org/10.1016/j.earscirev.2012.03.002

Sprain, C.J., Renne, P.R., Clemens, W.A., Wilson, G.P., 2018. Calibration of chron C29r: New high-precision geochronologic and paleomagnetic constraints from the Hell Creek region, Montana. Bull. Geol. Soc. Am. 130, 1615–1644. https://doi.org/10.1130/B31890.1

Sprain, C.J., Renne, P.R., Vanderkluysen, L., Pande, K., Self, S., Mittal, T., 2019. The eruptive tempo of deccan volcanism in relation to the cretaceous-paleogene boundary. Science (80-.). 363, 866–870. https://doi.org/10.1126/science.aav1446

Stachnik, J.C., Dueker, K., Schutt, D.L., Yuan, H., 2008. Imaging Yellowstone plume-lithosphere interactions from inversion of ballistic and diffusive Rayleigh wave dispersion and crustal thickness data. Geochemistry, Geophys. Geosystems 9. https://doi.org/10.1029/2008GC001992

Tsekhmistrenko, M., Sigloch, K., Hosseini, K., Barruol, G., 2021. A tree of Indo-African mantle plumes imaged by seismic tomography. Nat. Geosci. 14, 612–619. https://doi.org/10.1038/s41561-021-00762-9

Van Ark, E., Lin, J., 2004. Time variation in igneous volume flux of the Hawaii-Emperor hot spot seamount chain. J. Geophys. Res. Solid Earth 109, 1–18. https://doi.org/10.1029/2003JB002949

Waite, G.P., Smith, R.B., Allen, R.M., 2006. VP and VS structure of the Yellowstone hot spot from teleseismic tomography: Evidence for an upper mantle plume. J. Geophys. Res. Solid Earth 111, 1–21. https://doi.org/10.1029/2005JB003867

White, R.S., McKenzie, D., 1995. Mantle plumes and flood basalts. J. Geophys. Res. 100. https://doi.org/10.1029/95jb01585

Wignall, P.B., 2001. Large igneous provinces and mass extinctions. Earth Sci. Rev. 53, 1–33. https://doi.org/10.1016/S0012-8252(00)00037-4

Wilson, G.P., 2014. Mammalian extinction, survival, and recovery dynamics across the Cretaceous-Paleogene boundary in northeastern Montana, USA. Spec. Pap. Geol. Soc. Am. 503, 365–392. https://doi.org/10.1130/2014.2503(15)

Zhang, N., Zhong, S., Leng, W., Li, Z.X., 2010. A model for the evolution of the Earth's mantle structure since the Early Paleozoic. J. Geophys. Res. Solid Earth 115, 1–22. https://doi.org/10.1029/2009JB006896

Figures and Tables

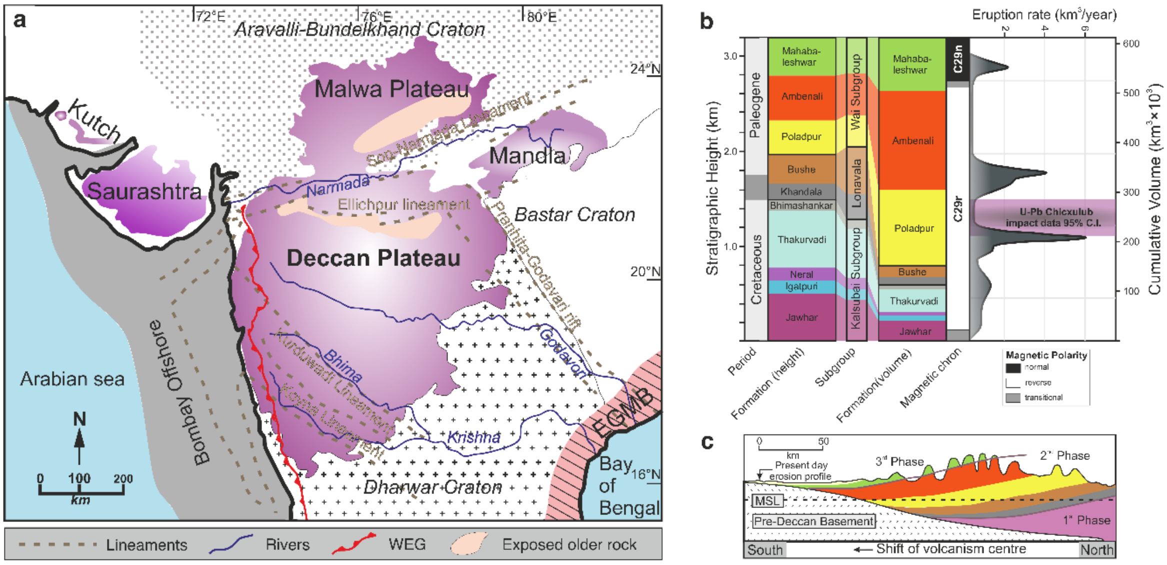

Fig. 1. Geology of the Deccan volcanic province (DVP). **(a)** Map showing the four main sub-provinces of DVP. The Deccan traps (DTs) rest on Precambrian basement rocks (shown in various legend patterns). The terrain contains a number of structural zones, such as lineaments and escarpment (marked as green dashed lines). Blue lines depict the major rivers flowing across DVP. WGE = Western Ghat Escarpment, EGMB = Eastern Ghat Mobile Belt. Reconstructed from (Kale et al., 2020) **(b)** Stratigraphic succession of the DVP (Left column) and their corresponding cumulative eruption volumes (Right column) along with ages for the three main subgroups of DVP in the Western Ghats (Renne et al., 2015). The panel shows the following elements (from left to right): cumulative stratigraphic height, geological time scale with the KPB indicated by the gray area, timescale of geomagnetic polarity with various magnetic chrons, and cumulative volume of Deccan lava. It also includes the probabilistic volumetric eruption rate and the Chicxulub impact time from Schoene et al., 2019 **(c)** A thematic geological cross-section of the DTs to illustrate the three major phases and their corresponding formations (Chenet et al., 2009). Color legends correspond to those used in (b).

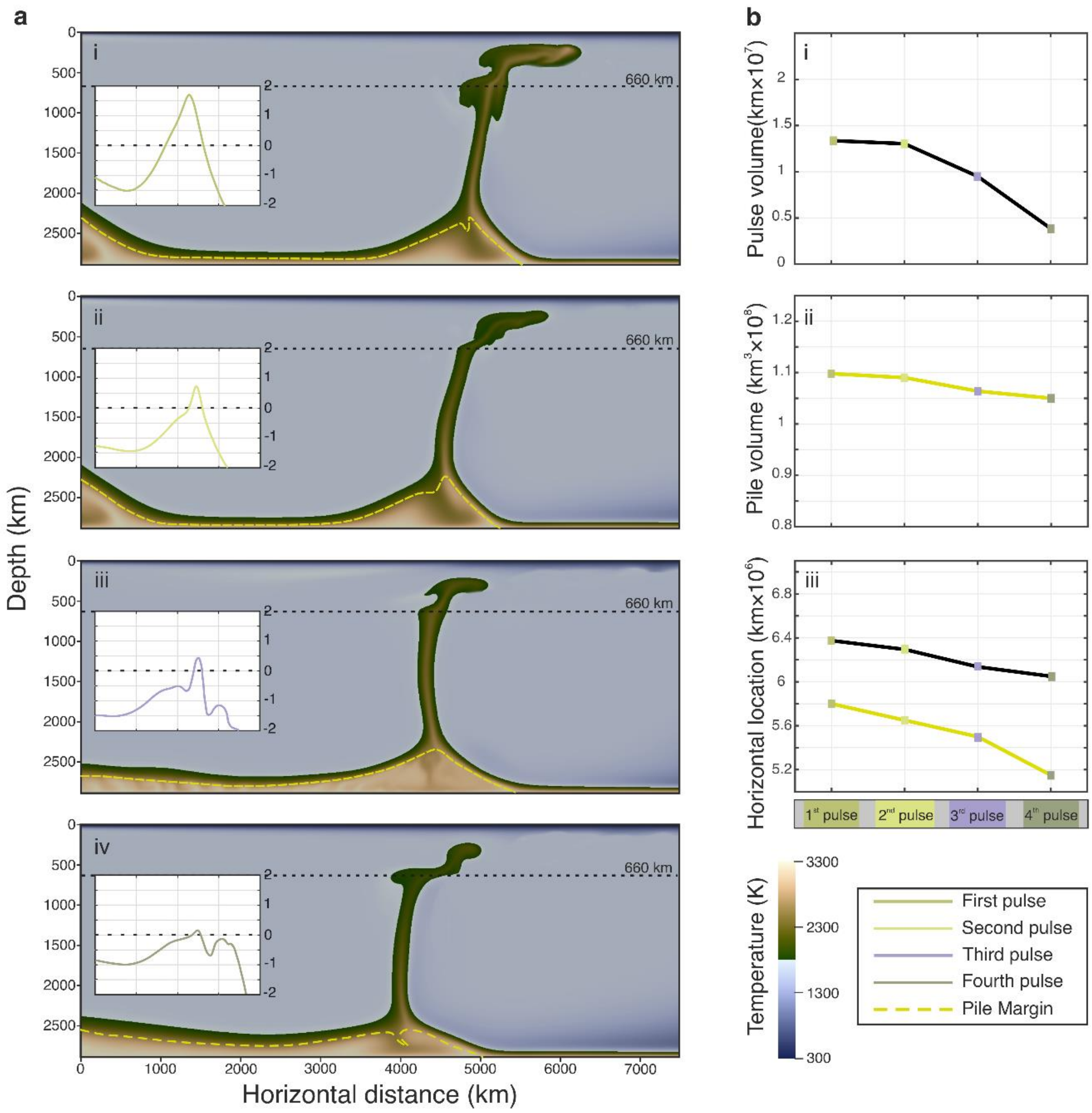

Fig. 2. Pulsating ascent dynamics of thermochemical plume at mid-mantle transition zone. (**a**) Development of successive four pulses (i-iv) from a thermochemical plume in models with buoyancy number (B) = 0.8, viscosity ratio (μ) = 100 and heat producing element concentration (c_{HPE}) same as the background mantle. Colors (Crameri et al., 2020) represent the temperature and dashed yellow lines delineate the pile margin. Insets show the dynamic topography (in km) corresponding to each pulse. **(b)** Calculated plots of the pulse volume **(i)**, the pile volume **(ii)**, and the locations of plume (black) and pile margin (yellow) **(iii)** during the four pulse events (denoted in different colors). The volumes are calculated based on the initial volume provided in Table 1.

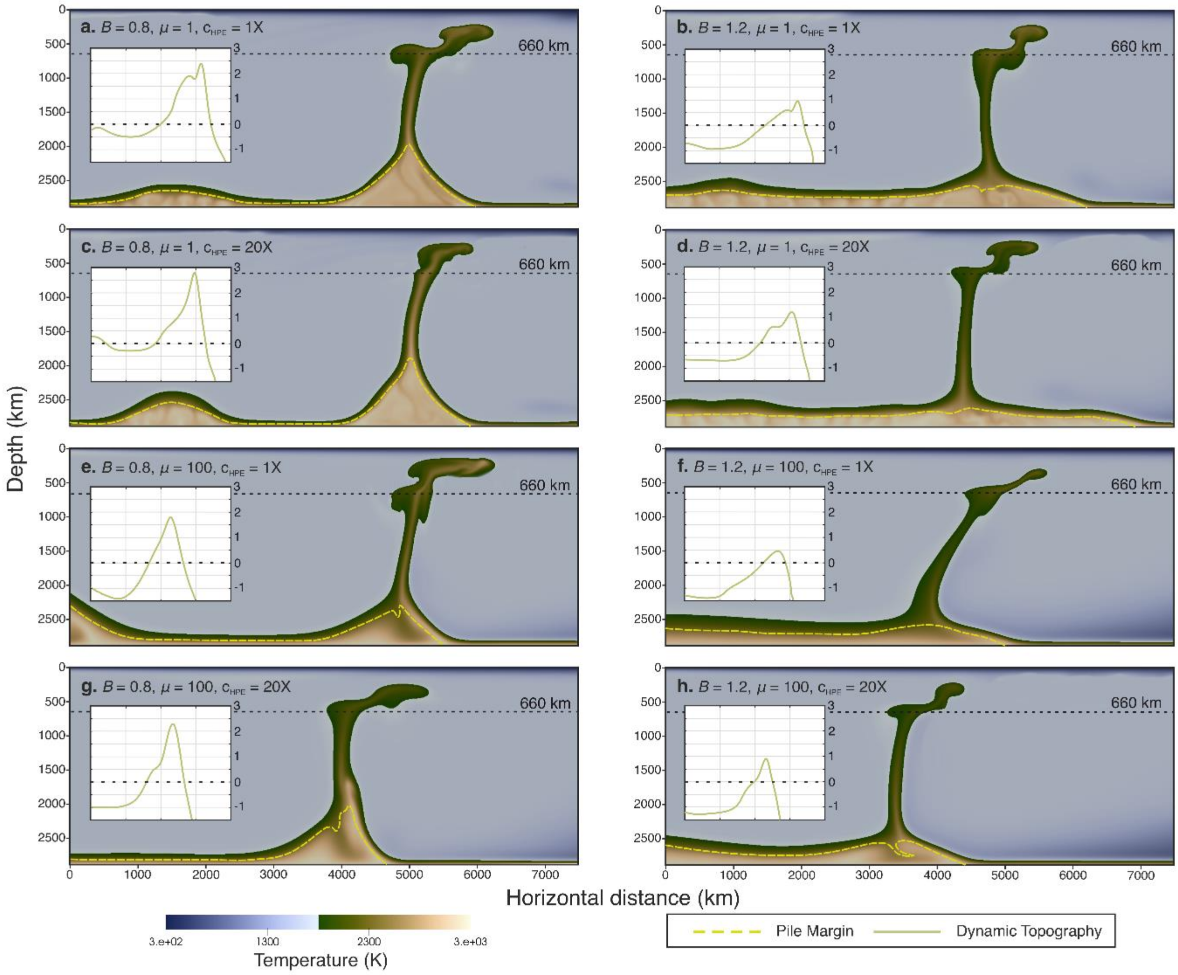

Fig. 3. Effects of the model parameters on pulse and pile dynamics**.** Geometry and locations of the pulses generated from a plume head and the pile in different models with varying parameters: **(a)** B = 0.8, μ = 1, and c_{HPE} = 1X; **(b)** B = 1.2, μ = 1, and c_{HPE} = 1X; **(c)** B = 0.8, μ = 1, and c_{HPE} = 20X; **(d)** B = 1.2, μ = 1, and c_{HPE} = 20X; **(e)** B = 0.8, μ = 100, and c_{HPE} = 1X; **(f)** B = 1.2, μ = 100, and c_{HPE} = 1X; **(g)** B = 0.8, μ = 100, and c_{HPE} = 20X; **(h)** B = 1.2, μ = 100, and c_{HPE} = 20X, where X denote c_{HPE} value for the background mantle. Color scale are same as in Fig. 2. Inset of each figure shows the dynamic topography (in km) at the surface for the pulses presented in the respective snapshot.

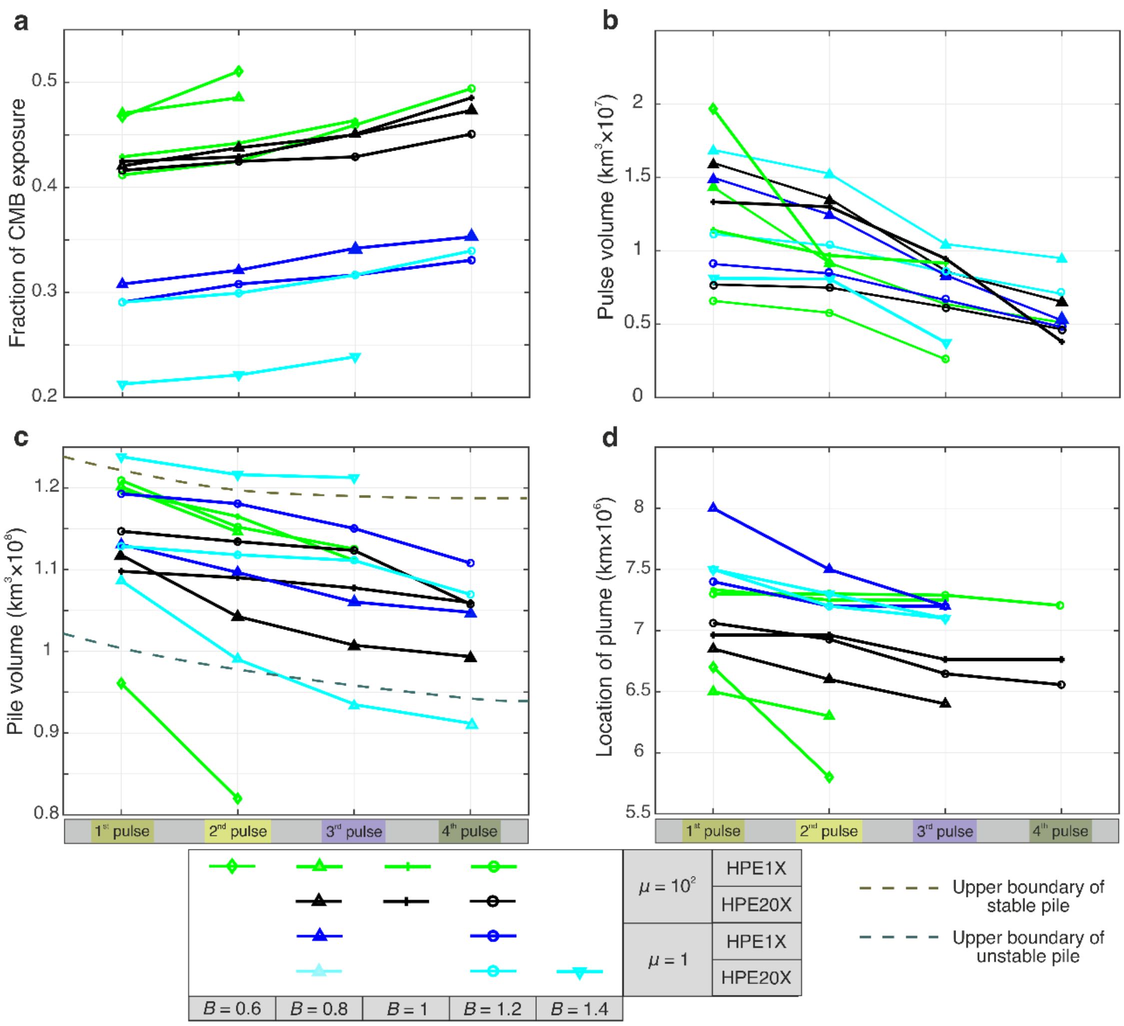

Fig. 4. Calculated plots from numerical models of successive pulses for different parametric values. (**a**) Variation in the exposed fraction of the core mantle boundary (CMB) for different model parameters. **(b) - (c)** Decreasing trends of successive pulse and pile volumes. **(d)** Varying plume head locations for successive pulses. The x-axis represents successive pulses, which in turn reflect progressive time. The symbols stand for the parameter *B*, and the colors denote μ and c_{HPE}. Their details are provided in the legend. Also provided are the fields of passive, stable and unstable piles using dashed curves.

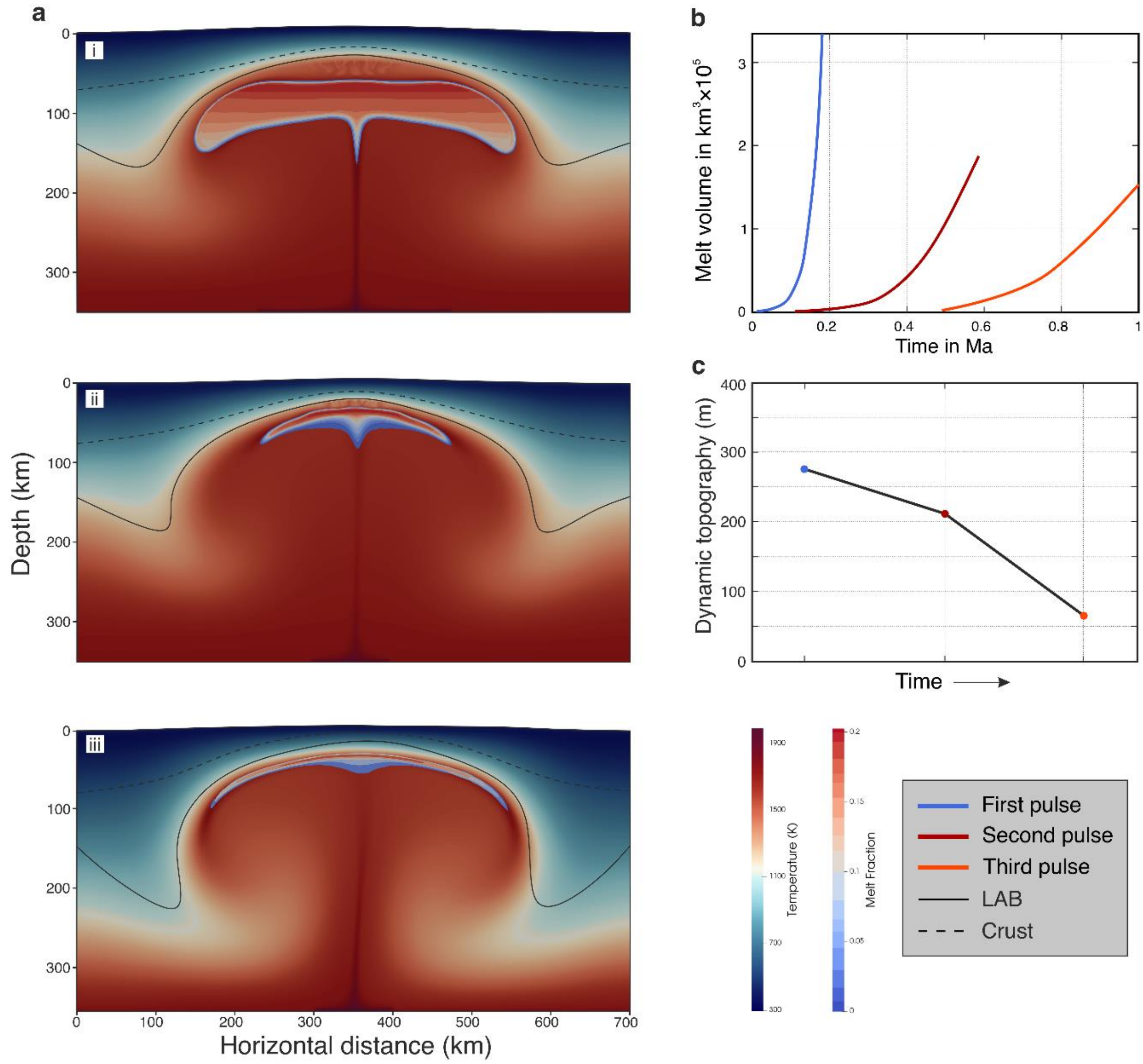

Fig. 5. Melt production by partial melting of plume head in the model. (**a**) Melt localization in three successive melt pulses (**i-iii**) at lithosphere-asthenosphere boundary (LAB). They originate from a single major pulse obtained from the whole mantle model. Colors represent the temperature and the colored contours represent melt fraction. Black line delineates the deformed LAB geometry. The slight tilt in the plume axis results from plate movement. The first two pulses (i-ii) involve intense thermal erosion at the contact between the melt front and the LAB, resulting in thinning of the thermal boundary layer. The top boundary is deflected to produce topography during the successive melting events. **(b)** Calculated plots of melt volume formed in successive melt pulses. **(c)** Melt-driven dynamic topography for three successive pulses. The colors used to represent the pulses in (b) and (c) are shown in the legend.

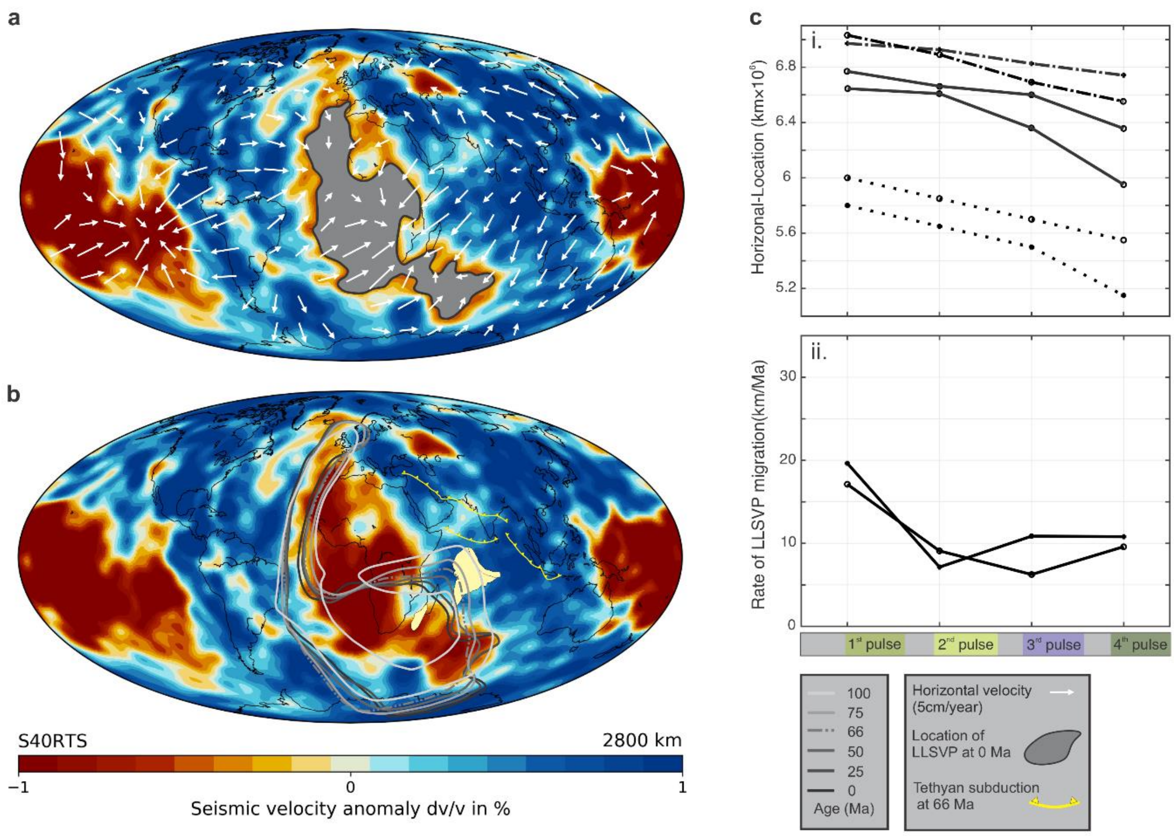

Fig. 6. African LLSVP and its connection to the Réunion hotspot and the Deccan volcanism. (**a**) Global map showing the present-day location of African LLSVP (gray shade) and the poloidal velocity components at a level 150 km above CMB constructed from Ford and Long, 2015. Strong south-westward velocity can be noticed at the eastern flank of the LLSVP. **(b)** Contours of 75% chemical concentration corresponding to a time series, 100 Ma to present day. The contour plots depict positional changes of African LLSVP through geologic time. The contours are redrawn from Hassan et al., 2016, 2020 expect that for 66 Ma (dashed contour) which is interpolated. The figure also shows location of the Tethyan subduction system and Indian plate (yellow) during the Deccan volcanism at 66 Ma. At this time the western margin of Indian plate was located directly above the eastern flank of the African LLSVP. The base map has been produced using S40RTS (Ritsema et al., 2011) depth slice at 2800 km on SubMachine. **(c)** Plots of the locations of African LLSVP (solid lines), Réunion plume tail (dotted lines) and plume head (dashed lines) **(i)**, the rate of southward migration of LLSVP, and **(ii)** those calculated from two of our representative models (see text) for each successive pulsation events.

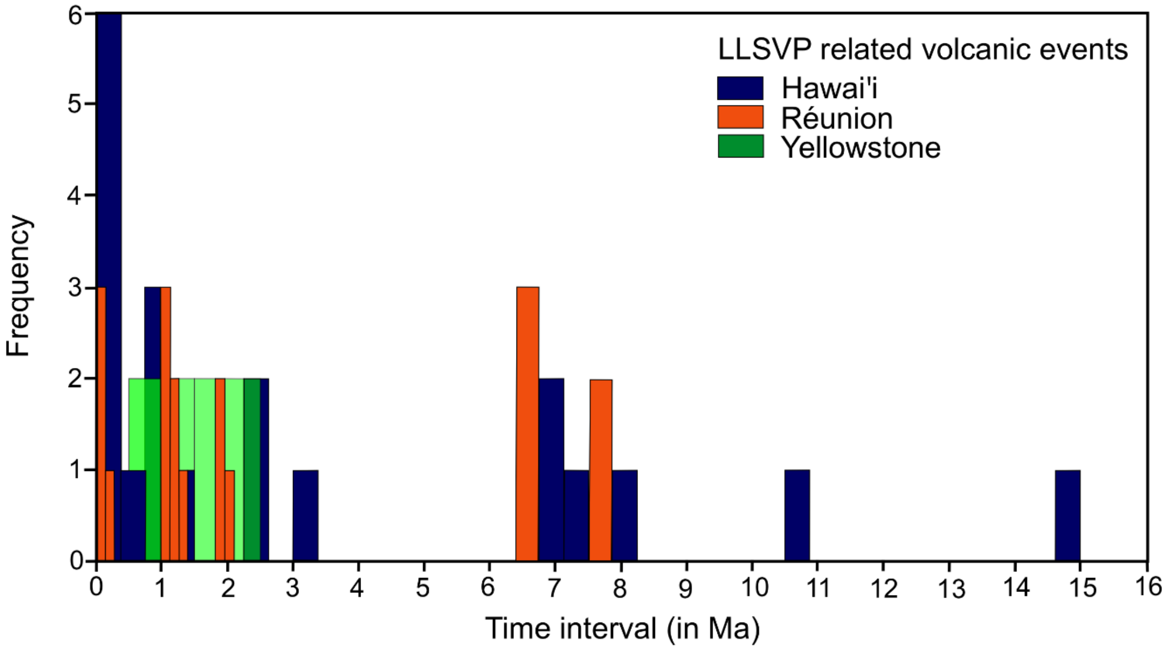

Fig. 7. A timescale analysis of global LLSVP related volcanic events. Histogram analysis of the periodic variations of volcanism in Hawai'i (Blue), Réunion (Saffron), and Yellowstone (Green). Short-term (< 1.5-2 Ma oscillations) and long-term (> 3 Ma oscillations) temporal variations are distinct in the plots (see discussion).

Table 1 Physical parameters and their values used for thermochemical modelling

Model Parameters	Reference values
Mantle thickness z_0	2890 km
Reference density ρ_o	3340 kg/m^3
Reference viscosity μ_o	2×10^{20} Pa s
Thermal conductivity k	4.1 W K^{-1}m^{-1}
Specific heat C_P	1250 J K^{-1} kg^{-1}
Thermal expansivity α_0	3×10^{-5} K^{-1}
Thermal boundary layer thickness at the CMB (h_{TBL})	100 km
Initial basal layer thickness h_{pile}	150 km
Basal layer density ρ_b	3730-3950 kg/m^3
Basal layer viscosity μ_b	$5 \times 10^{21} - 5 \times 10^{23}$ Pa s
Viscosity ratio $\mu^{\dagger}$	$0.1 - 10^2$
Top temperature T_{top}	300 K
Bottom temperature T_{bot}	3300 K
Reference Temperature T_{ref}	1600 K
Buoyancy number B	0.6 to 1.4
Background Heating rate X	6×10^{-9} W/kg
Basal layer heat producing element concentration (c_{HPE})	$1\mathrm{X} - 20\mathrm{X}$
Initial basal layer volume‡	3×10^8 km^3
Clapeyron slope at 660 km phase transition (γ_{660})	-2×10^6 Pa/K
Clapeyron slope at 410 km phase transition (γ_{410})	3×10^6 Pa/K

† Ratio of viscosity of the basal layer and the ambience

‡ Initial basal layer volume is calculated from the total volume of African LLSVP considering that the eastern flank (corresponds to the initial basal layer) comprises only a fraction of the total volume.

Table 2 Physical parameters and their values used to model partial melting in plumes

Model Parameters	Reference values
Melt density ρ_f	2700 kg/m^3
Reference shear viscosity η_o	5×10^{18} Pa s
Melt viscosity η_f	10 Pa s
Reference permeability k_0	5×10^{-9} m^2
Reference porosity ϕ_0	0.05
Melt weakening factor α	10
Thermal viscosity exponent β	5
Thermal expansion coefficient $\alpha_{thermal}$	3×10^{-5} K^{-1}
Solid compressibility κ_s	3×10^{-12} Pa^{-1}
Melt compressibility κ_f	3.8×10^{-11} Pa^{-1}
CFL number	1

Supplementary material for

Periodicity in the Deccan volcanism modulated by plume perturbations at the mid-mantle transition zone

Dip Ghosh, Joyjeet Sen, and Nibir Mandal*
Department of Geological Sciences, Jadavpur University, Kolkata 700032, India

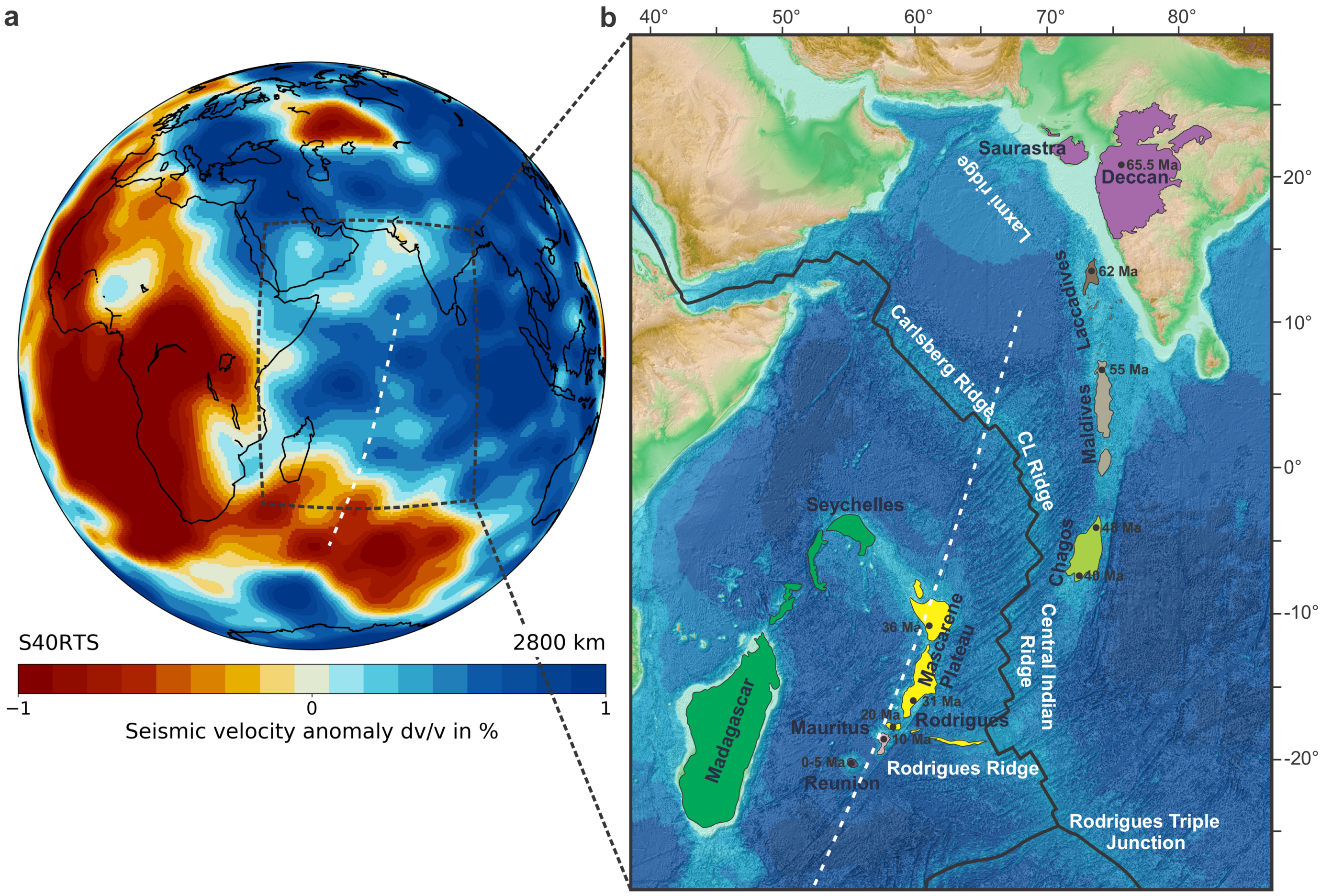

Fig. S1. Details of the study area in a global perspective. **(a)** Tomography-Depth slice at 2800 km, showing the present-day location of the eastern flank of African LLSVP using S40RTS model (data generated using SubMachine). **(b)** Satellite bathymetry map of the western Indian Ocean showing the complete Réunion hotspot track (Deccan Traps to Réunion Island). Aerial extent of the Deccan volcanic province is demarcated in purple within the Indian subcontinent. Crustal age estimates for Réunion plume activity (in Ma) indicate plume positions. Black lines delineate the plate boundaries. The base map is reproduced from BODC data. www.bodc.ac.uk. The white dashed line represents the trace of our model section.

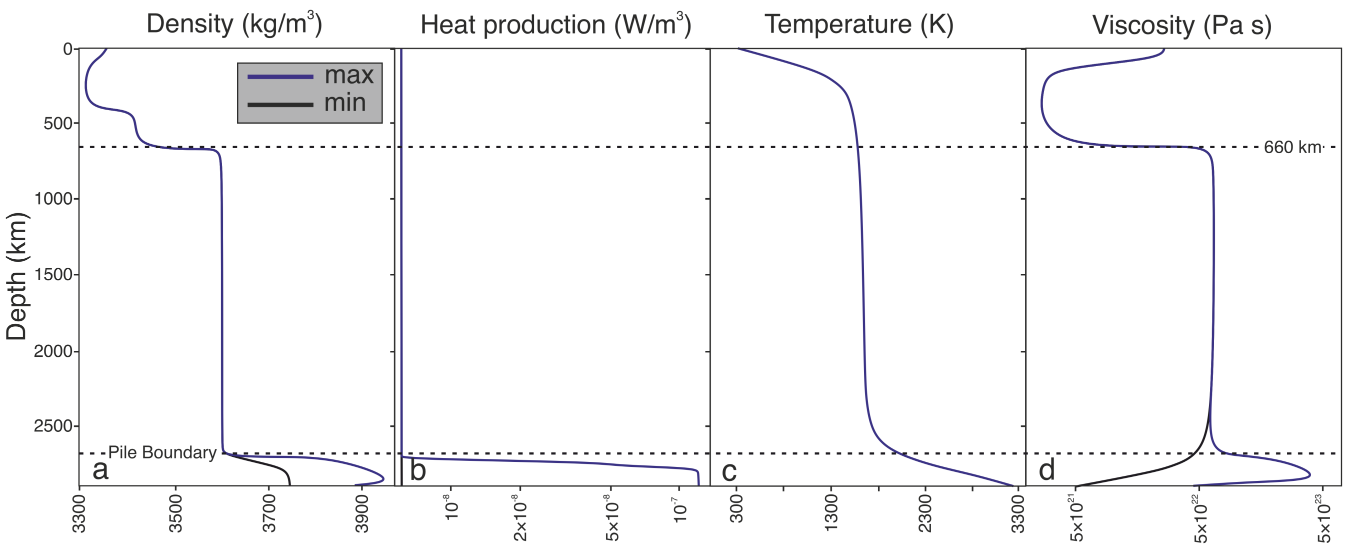

Fig. S2. Initial conditions considered for plume model simulations. **(a)** Initial density profile showing jumps of density values at the phase transition at 410 km and 660 km boundaries, and steep density increase near CMB due to the presence of a thermochemical pile. Blue and black lines indicate the maximum and minimum pile density considered in the modelling. **(b)** Depth profiles of the initial internal heat-production rate for the ambient mantle and the pile. The pile at CMB is enriched in heat-producing element (HPE) by up to 20 times relative to the ambient mantle. **(c)** Initial thermal structure of the mantle at the onset of convection, characterized by strong thermal boundary layers (TBL) at the upper 200 km (lithosphere) and at 100 km above the CMB. **(d)** Initial viscosity profile considered in our models. It accounts for both temperature and depth effects. The pile material is up-to 100 times (blue) more viscous that the ambient mantle.

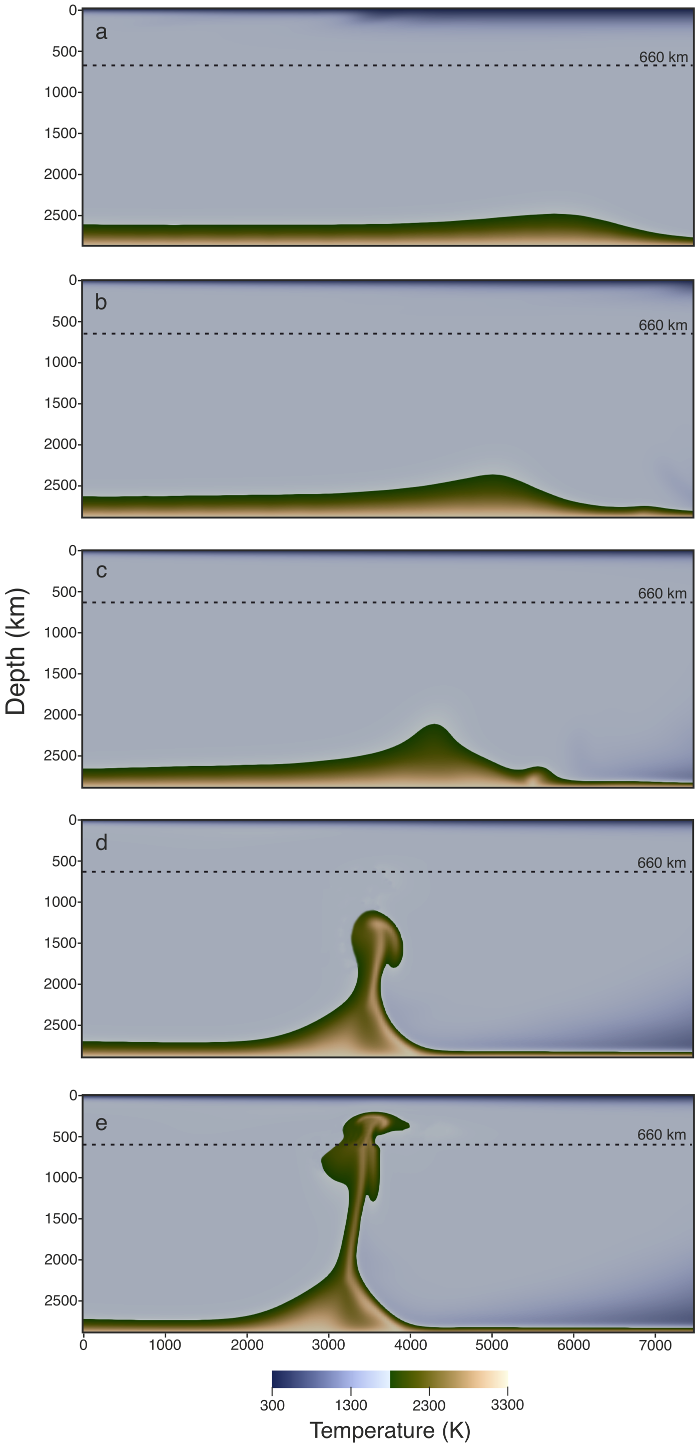

Fig. S3. Evolution of a thermochemical plume in the reference model ($B = 0.8, \mu = 100$, and $c_{HPE} = X$). **(a)** Piling up of TBL due to forcing by a downwelling flow in mantle. **(b)** Growth of a small instability on the extreme right side of the TBL. **(c)** Lateral advection and climb of the instability to the pile crest. **(d)** Development of a mature plume from the instability with increasing buoyancy flux. **(e)** Perturbation of the plume head at the mid mantle transition zone to produce a primary pulse. Note that the pulse in the upper mantle deflect to the right under the influence of plate velocity.

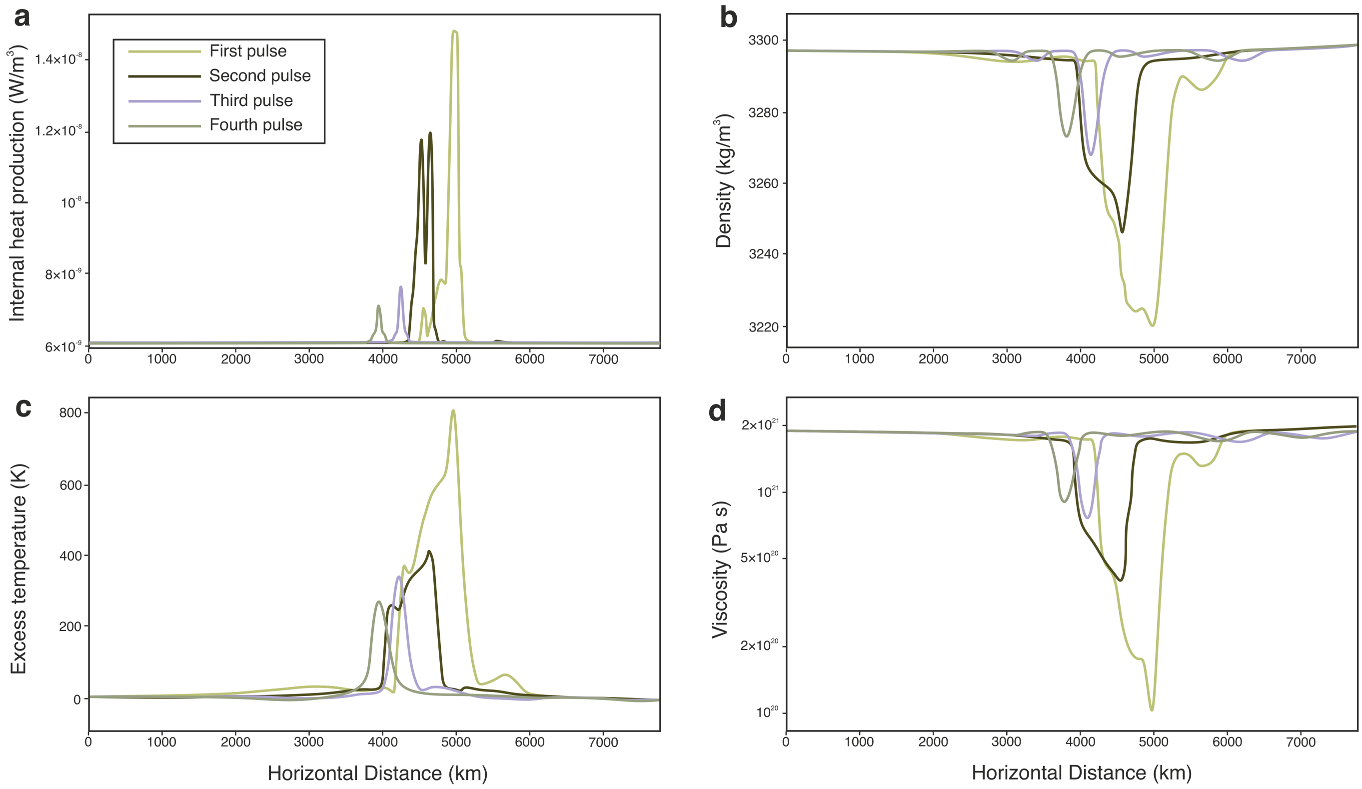

Fig. S4. Horizontal variation of the physico-chemical properties in four successive plume pulses produced at the mid-mantle transition zone. The graphical plots correspond to a depth of 400 km. **(a)** Variations of internal heat production showing a maximum peak value for the first pulse (yellow curve). Note that the next pulses consistently reduce their peak values. The secondary pulse (Brown) contains considerable amount of HPE, as reflected from its high internal heating production, which weakens with the tertiary pulses (blue and green curves). Their reducing trend indicates decrease in HPE concentration due to less entrainment of pile materials by the plume. **(b)** Density profiles. The first pulse show the highest negative density anomaly reflecting strong buoyancy head. The density anomalies significantly weaken in the secondary and tertiary pulses. **(c)-(d)** Excess temperature and viscosity profiles for the pulses, the patterns of which agree with the HPE concentration and the density profiles in (a) and (b), respectively.

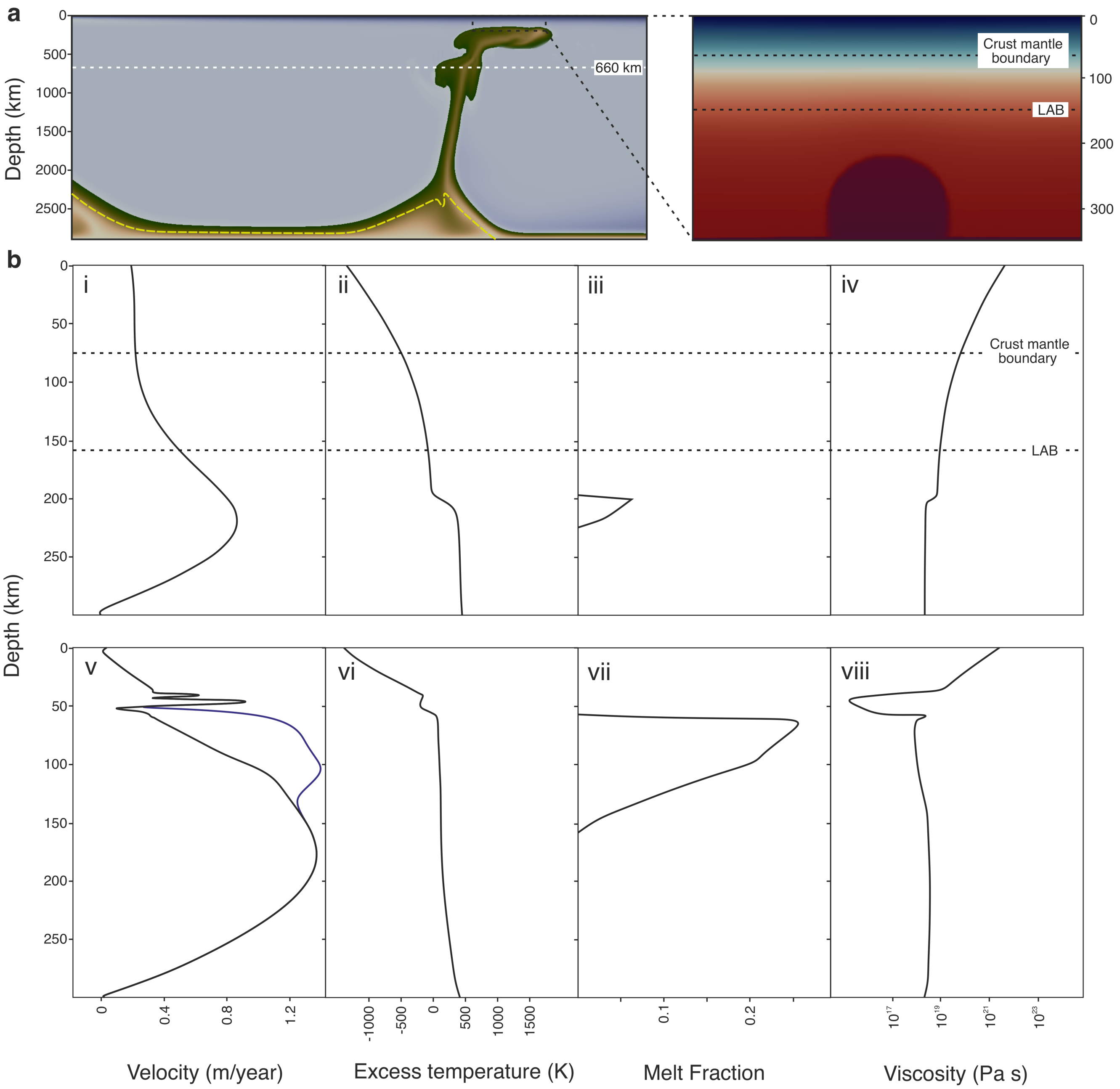

Fig. S5. Model simulations of the melt transport processes. **(a)** Model domain (inset) chosen within the plume model (left panel). **(b)** Depth dependent variations of the physical parameters: flow velocity, excess temperature, melt-fraction and viscosity at the time of melt initiation **(i-iv)** and at the onset of thermal erosion of the lithosphere by the partial melts **(v-viii)**.

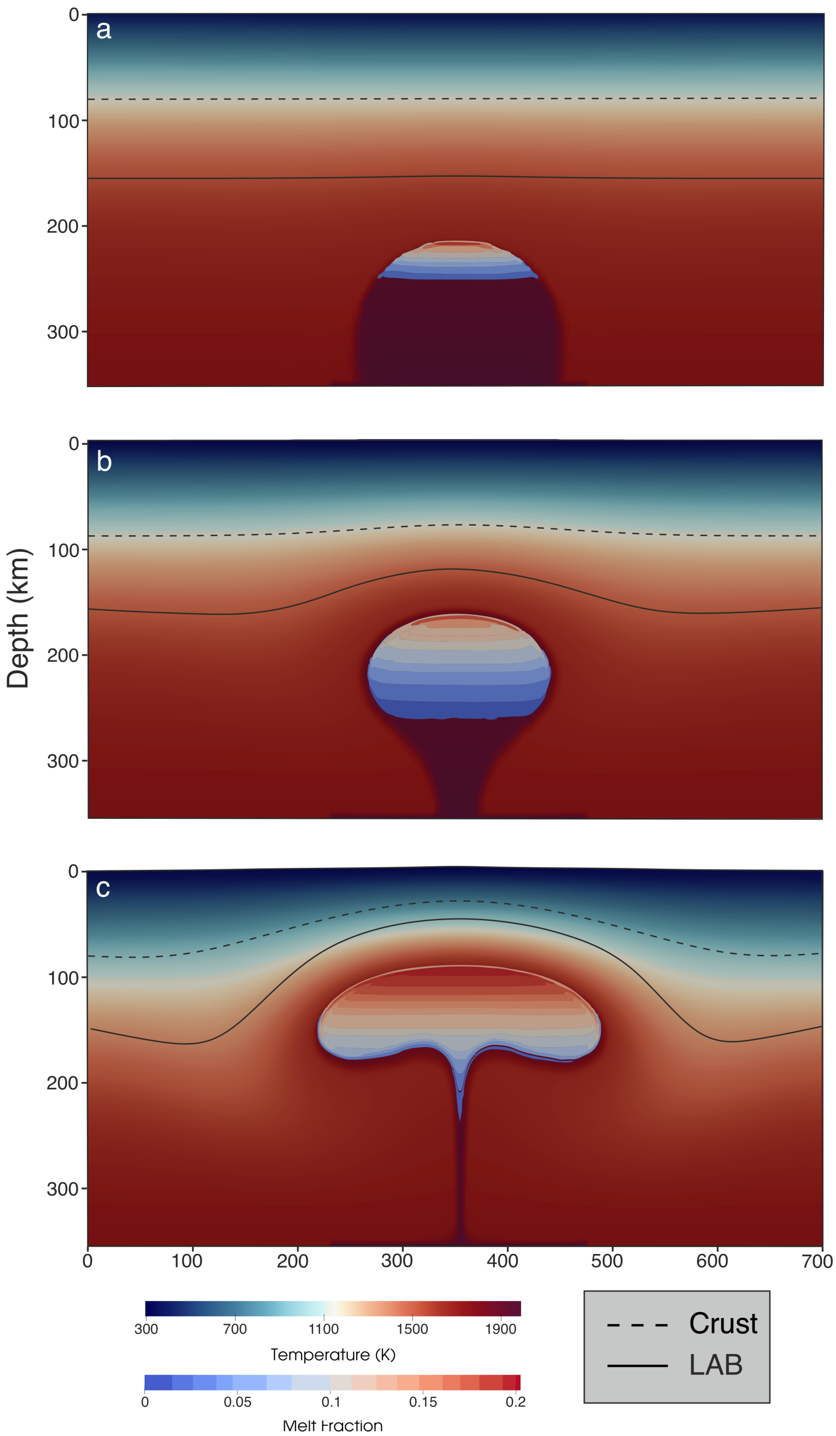

Fig. S6. Time evolution of models showing melt production by partial melting. **(a)** Melt initiation at the crest of the plume head. **(b)-(c)** Progressively increasing melt fraction as the plume head interacts with the LAB.